Compression-softening effect in prestressed beams: Experimental–finite-element vibration analysis of post–tensioned thin-walled steel-box-girders

Marco Bonopera[a,*], Kuo-Chun Chang[a], Nerio Tullini[b]

[a]*Dept. of Civil Engineering, National Taiwan University, No. 1, Sec. 4, Roosevelt Rd., Taipei, 10617, Taiwan*

[b]*Dept. of Engineering, University of Ferrara, No. 1, Via Saragat, Block A, Ferrara, 44122, Italy*

*Corresponding author – Email: marco.bonopera@unife.it

In published works, there is a discrepancy about the effect of pre and post–tensioning forces on the beam dynamics. Particularly, the dynamic effects caused by an external compressive force and that due to post–tensioning appear to be quite different. To solve this conflict, free transverse vibrations of a simply supported post–tensioned thin-walled steel-box-girder were investigated. Its fundamental frequencies were then measured for different values of post–tensioning force. Subsequently, the experimental data were compared with a formula taking shear effects into account. The experimental data were also compared with two high-fidelity finite-element models. According to the findings of this study, and comparisons with several tests reported in the literature, the beam dynamics due to a compressive force and that caused by post–tensioning is different only when the cables are in contact with the surrounding beam's section. Depending on this feature, the dynamics of pre and post–tensioned beams is ruled by compression-softening effect. Moreover, in thin-walled steel-girder-bridges draped with a deviator, the fundamental frequency as indicator for post–tensioning loss identification is made doubtful.

Keywords: Finite-element model; Frequency; Post–tensioning; Shear deformation; Straight cable; Thin-walled box-girder

1. Introduction

Prestressing techniques were widely used for realizing important structures and infrastructures owing to their superior performance and high durability. The prediction of change in natural vibration frequencies with varying prestressing force in beams is a crucial problem, see Bai-jian et al. [1], Gan et al. [2] and references cited therein. Structural engineers should be able to estimate changes in natural frequency of prestressed structures over the course of their design life to ensure their safety. This argument is significant in the field of bridges and wind turbine towers, both of which are susceptible structures to dynamic excitation [3, 4]. E.g., vibration measurements, taken during the operation stage of a concrete bridge or a prestressed steel wind tower, are useful applications to control their calculation model, evaluate their stiffness or monitor their internal stresses [5, 6]. Bonopera et al. [7] fully illustrated a state-of-the-art review of researches conducted worldwide about this topic. Particularly, Hamed and Frostig [8], Jaiswal [9], Limongelli et al. [10] and Bonopera et al. [11, 12] declared that the natural frequencies and stiffness of Prestressed Concrete (PC) girder-bridges, with a parabolic or a straight tendon, only significantly vary under the effect of crack initiation or crack re-opening. Pisani et al. [13] confirmed that, for prestressed beams, modal parameters provide information regarding damage only when the members are close to the ultimate conditions. Previously, Noble et al. [14, 15] executed several experiments on a number of post–tensioned steel and concrete beams in small-scale. The researchers declared that the small reduction in fundamental frequency with increasing post–tensioning force is not related to the softening effect. Thus, they deduced that the compression-softening theory must be eliminated from discussion of all forms of pre and post–tensioned structures. The researchers also claimed that the dynamic effect of a compressive force and that of a post–tensioning on a beam are different on a phenomenological level. Consequently, they retained that a prestressing force should always be considered as an axial force internally applied. Gan et al. [2] sustained that this divergence in Noble et al. [15] was caused by the closure effect of shrinkage cracks and/or microcracks inside the post–tensioned concrete beams which, in turn, was not considered in the theoretical predictions of fundamental frequency. According to the literature above mentioned, there is a meaningful disagreement among researchers about the effect of pre and post–tensioning forces on the beam dynamics. Therefore, it was deemed that the results regarding this topic need additional experimental investigations on steel beams rather than those in reinforced concrete, with the aim to prevent stiffening effects caused by the microcrack closure [9] and by the time-increment of Young's modulus regarding the consolidation/hardening of concrete [11, 12, 16]. Such investigations had to be conducted on post–tensioned beams in a larger scale for avoiding that any mass at the end constraints, usually composed of load cells and/or hydraulic jacks, was greater than the self-mass of the beams themselves. In fact, it is what occurred in Noble et al. [14] where the fundamental frequencies were affected by such masses [11, 12]. Accordingly, the conclusions of Noble et al. [14] required to be revised.

Hence, this work was mainly necessary for properly clarifying and evaluating the dynamics of prestressed beams. Indeed, a correct evaluation of fundamental frequency is crucial for designing new bridges and prestressed wind turbine towers, monitoring and determining the conditions of existing ones and related components. Furthermore, the reproduction of experimental data using correct algorithms enables effective interpretations of in situ measurements and simulations of virtual laboratory tests [17].

This work was a research sub-program developed at the National Center for Research on Earthquake Engineering (NCREE) according to a campaign study on girder-bridges which initiated in 2015 by testing PC beam specimens [11, 12, 16–20]. Given the conflicts in the aforementioned findings, firstly, free transverse vibrations were induced to a simply supported post–tensioned thin-walled steel-box-girder in larger scale and with eccentric straight cables. Different post–tensioning forces were applied. The specimen was characterized by initial second-order curvatures, due to the post–tensioning force causing two equal bending moments at the end constraints, and an axial end constraint, due to the stiffness of the cables [21, 22]. Secondly, the experiments executed by Noble et al. [14] were analyzed. Indeed, the researchers similarly investigated the compression-softening theory in two simply supported thin-walled steel-box-members post–tensioned by a straight cable. The two specimens in small scale had different slenderness. Subsequently, the fundamental frequencies measured from testing, and those obtained by Noble et al. [14] ‘s experiments, were compared with a formula based on the Timoshenko shear beam model [23], where the post–tensioning force is equivalent to a compressive force externally applied. The frequencies were also compared with two high-fidelity Finite-Element (FE) models including shear deformation, in which the post–tensioning force is applied as initial tension in the cables. In the FE analyses, the contact between cables and surrounding sections was additionally simulated. According to the obtained findings, the dynamic effect of a compressive force and that of a post–tensioning are phenomenologically different only when the cables are in contact with the surrounding beam's section. Depending on this feature, the dynamics of all forms of pre and post–tensioned beams is ruled by compression-softening effect. Similarly to what deduced for PC girder-bridges [7, 19, 20], the fundamental frequency as parameter for post–tensioning loss identification is made doubtful in thin-walled steel-girder-bridges draped with a deviator.

2. Reference solutions

The reference solution, proposed in this study, describes the prestressed beam dynamics based on Timoshenko beam model, where transverse shear deformability is considered [23, 24]. The shear beam theory is often used to model the behavior of structures both for stability or dynamic analyses [25–27]. The effect of rotational inertia is neglected because it may be appreciable only at high frequencies [28]. Particularly, the vibrational response of an axially unloaded simply supported beam takes first-order effects into account including shear deformation [29]. Vice versa, an externally compressed member of length L allows to consider the second-order effects in a beam pre or post–tensioned by a straight tendon which can be or not in contact with the surrounding section (Fig. 1). This configuration characterized the experimental investigations illustrated in Section 3.1. Indeed, a thin-walled steel-box-girder was subjected to different post–tensioning forces ($N_{0x,\mathrm{aver}}$) exerted by eccentric straight cables which, in turn, were free to vibrate inside the Rectangular Hollow Section (RHS) [30] (Sections 3.2 and 3.3). In short, the cables were only in contact at the girder ends. Their cross sectional area were assumed as unchanged after deformations. Therefore, the eccentricity (e) of post–tensioning forces ($N_{0x,\mathrm{aver}}$) was theoretically zero. The flexural shape $v^{(0)}$ of the girder's fundamental frequency ($f_{\mathrm{shear},1,II}$), with total self-mass per unit length m_{tot}, is represented in Fig. 1, according to the shear beam model which, in turn, included the second-order effects.

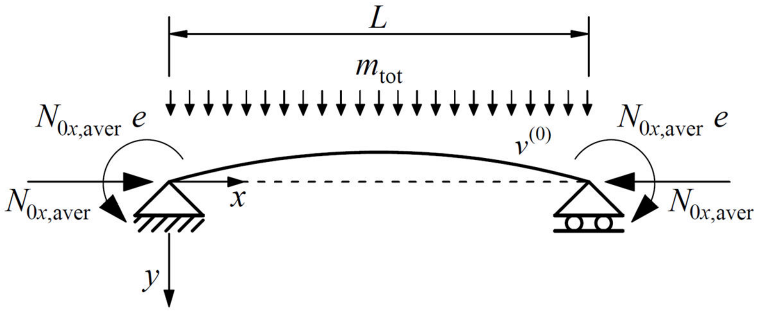

Fig. 1. Reference solution. Prismatic beam pre or post–tensioned by eccentric straight tendon. Fundamental flexural shape $v^{(0)}$ according to the shear model. The dashed line represents the undeformed configuration.

When the member in Fig. 1 meets all the requirements of Euler-Bernoulli theory, it is subjected to small displacements and rotations. Thus, the second-order nth natural frequency ($f_{\mathrm{E.\text{-}B.},n,II}$) of a simply supported post–tensioned steel-girder with a straight unbonded tendon is described by the following equation where, the effects of longitudinal vibrations and warping are not considered [23, 29]:

$$f_{\mathrm{E.\text{-}B.},n,II} = \frac{1}{2\pi}\sqrt{\frac{\alpha^2 n^4 \pi^4}{L^4}}\sqrt{1-\frac{N_{0x,\mathrm{aver}}}{N_{\mathrm{crE},n}}}\,. \qquad n = 1, 2, \ldots \tag{1}$$

Here the coefficient $\alpha^2 = EI\,g\,/m_{\mathrm{tot}}$ contains Young's modulus E and cross sectional second moment of the area I of the thin-walled box-girder. The gravitational acceleration g = 9.81 m/s^2. Instead, the second square root contains the nth critical buckling load of the simply supported girder given by $N_{\mathrm{crE},n} = n^2\,\pi^2\,EI\,/L^2$. The self-mass per unit length of the straight unbonded tendon (m_{tendon}) does not affect the beam dynamics. Likewise, no stiffening effect is induced by the cables under post–tensioning ($N_{0x,\mathrm{aver}}$). Assuming n = 1 in Eq. (1), the second-order fundamental frequency ($f_{\mathrm{E.\text{-}B.},1,II}$) is obtained. In detail, Eq. (1) reduces to Eq. (2) reported in Bonopera et al. [11], where the nth critical buckling load ($N_{\mathrm{crE},n}$) becomes equal to the Euler buckling load $N_{\mathrm{crE},1} = \pi^2\,EI\,/L^2$. Furthermore, disregarding the term containing the post–tensioning force $N_{0x,\mathrm{aver}}$, Eq. (3), likewise reported in Bonopera et al. [11], is achieved. Such formula represents the first-order fundamental frequency ($f_{\mathrm{E.\text{-}B.},1,I}$) of simply supported PC girder-bridges with a straight bonded or unbonded tendon. Indeed, the dynamic effect of a pre or post–tensioning force ($N_{0x,\mathrm{aver}}$) is negligible in these types of PC girder-bridges [11]. Conversely, when the aforementioned thin-walled girder meets all the requirements of the shear beam model, its first-order nth natural frequency ($f_{\mathrm{shear},n,I}$) is expressed by the following equation which, in turn, does not consider longitudinal vibrations, warping and rotary inertia [29]:

$$f_{\mathrm{shear},n,I} = \frac{1}{2\pi}\sqrt{\frac{\alpha^2 n^4 \pi^4}{L^4\left(1+\frac{n^2\pi^2 r^2}{L^2}\frac{E}{k\,G}\right)}}\,. \qquad n = 1, 2, \ldots \tag{2}$$

In Eq. (2), the coefficient $r^2 = I\,/A$, where A is the cross sectional area of the thin-walled girder. Elastic shear modulus $G = E\,/\,[\,2\,(1+\upsilon\,)\,]$. υ is Poisson's ratio. k is instead the shear coefficient for generic thin-walled hollow sections which is described by the following equation [31]:

$$k = \frac{10(1+\upsilon)(1+3\mathrm{m})^2}{\left(12+72\mathrm{m}+150\mathrm{m}^2+90\mathrm{m}^3\right)+\upsilon\left(11+66\mathrm{m}+135\mathrm{m}^2+90\mathrm{m}^3\right)+10\mathrm{n}^2\left[(3+\upsilon)\mathrm{m}+3\mathrm{m}^2\right]}\,. \tag{3}$$

Here we have the parameters $\mathrm{m} = b\,t_{\mathrm{I}}\,/\,h\,t$ and $\mathrm{n} = b\,/\,h$, where internal width b, thickness of the flanges t_{I}, height h, and thickness of the web t. According to the above, based on the shear model, and when second-order effects are assumed, the nth natural frequency ($f_{\mathrm{shear},n,II}$) of a simply supported post–tensioned thin-walled steel-girder with a straight unbonded tendon (Fig. 1) can be expressed as:

$$f_{\mathrm{shear},n,II} = \frac{1}{2\pi}\sqrt{\frac{\alpha^2 n^4 \pi^4}{L^4\left(1+\dfrac{n^2\pi^2 r^2}{L^2}\dfrac{E}{k\,G}\right)}}\sqrt{1-\frac{N_{0x,\mathrm{aver}}}{N_{\mathrm{crE,shear},n}}}. \qquad n = 1, 2, \ldots \tag{4}$$

In Eq. (4), the second square root, originating from Eq. (1), contains the nth critical buckling load with the effect of shear deformation ($N_{\mathrm{crE,shear},n}$) which is given by the following approximate formula [23]:

$$N_{\mathrm{crE,shear},n} = \frac{N_{\mathrm{crE},n}}{1+\left(N_{\mathrm{crE},n}/GA_0\right)}. \qquad n = 1, 2, \ldots \tag{5}$$

In Eq. (5), the nth critical buckling load of a simply supported girder $N_{\mathrm{crE},n}$, whereas the parameter $A_{\mathrm{o}} = A/m$. m is the correction coefficient which takes into account the nonuniform distribution of the shear stresses throughout the cross sectional area (A). For a generic thin-walled section, which bends in the plane of the web, $m \simeq A/A_w$. A_w is the cross sectional area of the web. Substituting $N_{\mathrm{crE},n} = n^2\pi^2 EI/L^2$ for the denominator, and the expression $I = r^2 A$ then, Eq. (5) can be reformulated by Eq. (6) which is reported as follows [23]:

$$N_{\mathrm{crE,shear},n} = \frac{N_{\mathrm{crE},n}}{1+n^2 m\left[\pi/(L/r)\right]^2 (E/G)}. \qquad n = 1, 2, \ldots \tag{6}$$

We see that the smallest critical buckling load ($N_{\mathrm{crE,shear},n}$) occurs for $n = 1$. When slenderness (L/r) is sufficiently large, shear effects are negligible, and the classical Euler solution is recovered. From Eq. (6) we observe that shear strains decrease the critical load ($N_{\mathrm{crE,shear},n}$). Therefore, the shear correction becomes significant for short post–tensioned thin-walled girders (small L/r) made with a high strength steel, so that the short beam still fails due to buckling rather than yield [23].

3. Experimental investigation

3.1. Thin-walled steel-box-girder post–tensioned by eccentric straight cables

Given the discrepancies created about the effect of pre and post–tensioning forces on the beam dynamics (Section 1), a thin-walled RHS member of $b = 150$ mm, $h = 350$ mm, $t = t_1 = 9$ mm, and made with a high strength steel, was adopted (Fig. 2). Steel was chosen to prevent any stiffening effects caused by the crack and/or microcrack closure [2, 9] and by the time-increment of Young's modulus regarding the consolidation/hardening of concrete [11, 12, 16]. The member was subjected to a series of post–tensioning forces exerted by a straight unbounded tendon with a small eccentricity ($e/h = 0.23$) with respect to the

RHS centroid (Fig. 2). The tendon was composed of 5 steel "seven–wire" strands, of 15.2 mm in diameter, which passed internally through the RHS body and only anchored at its ends (Fig. 2). The tendon's self-mass per unit length ($m_{\text{tendon}} = \rho_{\text{tendon}} \times A_{\text{tendon}}$) was 0.0533 kN/m. Two steel supports were arranged at the RHS ends to create pinned-end restraints, resulting in a clear span L (Fig. 2). $132 \times 176 \times 6$ mm^3 vertical stiffeners, made with the same structural steel, were welded into the RHS upper part at a distance of ≈ 1.0 m to prevent instability modes with respect to the girder's vertical axis under post–tensioning (Fig. 2). Furthermore, the RHS ends were covered by a 250×450×20 mm^3 steel plate, likewise made with the same steel. 12 threaded bars, of 16 mm in diameter, were utilized for the fastening, for a total mass at the RHS ends of 317.1 N [Figs. 3(a)–(b)]. All corresponding material and geometric properties of the thin-walled RHS member were listed in Table 1. Notably, unit weight, Young's modulus and yielding stress of high strength steel were evaluated by tensile tests considering the average values obtained from 4 hourglass specimens [32].

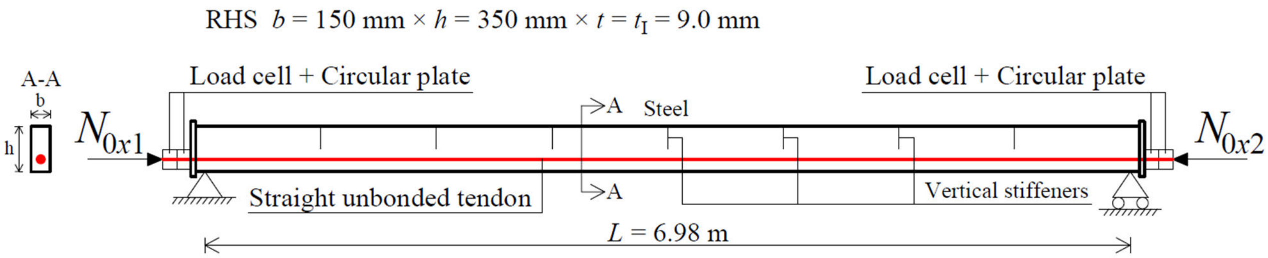

Fig. 2. Thin-walled steel RHS member post–tensioned by eccentric straight unbonded cables.

Table 1. Properties of the thin-walled steel RHS member (Fig. 2).

Property	RHS 50 × 30 × 3 mm^3
I (mm^4)	1.33399×10^8
A (mm^2)	8,676
A_w (mm^2)	5,976
Slenderness	56
k [Eq. (3)]	0.687
L (m)	6.98
ρ_{beam} (kN/m^3)	77.01
E (GPa)	205.12
f_{yk} (MPa)	390
G (GPa)	82.05
υ	0.25
A_{tendon} (mm^2)	695
ρ_{tendon} (kN/m^3)	76.65
E_{tendon} (GPa)	200
σ_{uy} (MPa)	1,860
e (mm)	80

(a) (b) (c)

Fig. 3. (a) Laboratory test rig. (b) Load cell and circular plate at one RHS end. Reference seismometer (Af) to the floor (Fig. 4). (c) Seismometer A1 on the top of quarter cross section (Fig. 4).

3.2. Experimental set-up

The thin-walled steel-box-girder was located in a test rig [Fig. 3(a)]. At one end constraint, a hydraulic jack, of 1,000 kN in force capacity, was utilized to apply the post–tensioning forces by pulling the cables outward (Fig. 2). Yet, a load cell, of 130 mm in diameter, 120 mm in length, 1,000 kN in force capacity, 2 mV/V in sensitivity, and 78.5 N in mass, was fixed at either RHS ends to measure the applied post–tensioning forces N_{0x1} and N_{0x2} [Fig. 2 and Fig. 3(b)]. A circular steel plate, of 130 mm in diameter, 60 mm in length, and 49.4 N in mass, was additionally located between the load cells and the end of cables [Fig. 3(b)]. 6 mean post–tensioning forces ($N_{0x,\text{aver}}$) were totally applied in values of ≈ 117, 214, 332, 421, 501 and 598 kN, to respectively induce second-order effects of 2.2, 4.0, 6.4, 8.2, 9.9 and 12.1% of the girder's critical buckling load $N_{\text{crE},1}$ or $N_{\text{crE,shear},1} = 5{,}543$ kN. Notably, the maximum tension force in each cable was not to exceed the value of ≈ 140 kN, according to the laboratory's safety conditions. Thus, the maximum tensile strength reached in the tendon, $\sigma_{\text{tendon,max}} = N_{0x,\text{aver,max}} / A_{\text{tendon}} = 598 \text{ kN} / 695 \text{ mm}^2 = 860$ MPa, was ≈ 46% of yielding stress σ_{uy} (Table 1). The different post–tensioning forces (N_{0x1} and N_{0x2}) measured at the RHS ends occurred because of the post–tensioning losses due to anchorage slips and relaxation of cables (Fig. 2). The measuring system included 5 seismometers installed along the RHS body (Af, A0, A1, A2 and A3) as depicted in Fig. 4. Particularly, 5 high–precision servo velocity seismometers, lightweight (2.65 N), of 50 mm in diameter, 70 mm in length, and 5 mV/gal in sensitivity, were selected (VSE–15D, Tokyo Sokushin). 2 seismometers of which, marked as A1 and A2, were vertically fixed on the top of quarter and midspan cross sections, i.e., at i = 1 and 2, with the aim to respectively collect acceleration data with respect to the RHS strong axis [Fig. 3(c) and Fig. 5(c)]. Vice versa, the 2 seismometers, marked as A0 and A3, were located on the top of the RHS ends (Fig. 4). The seismometer Af was instead placed as a reference to the floor, i.e., near the RHS end at i = 0 [Fig. 3(b)].

Af was used to record eventual anomalies of the measuring system. All seismometers were connected to a signal conditioner and, later, to a data logger placed on a desk near the test rig. The experimental set-up in Fig. 4 shows their positions in violet. The thin-walled box-girder's self-mass per unit length (m_{beam}), comprehensive of 4 seismometers (A0, A1, A2 and A3) and horizontal steel plates for positioning a number of displacement transducers, was 0.7167 kN/m. Specifically, such plates, of 300 × 120 × 7.5 mm^3 in dimension, 200 mm in length, and made with the same structural steel of the member, were welded along the RHS body [Figs. 5(a)–(b) and Fig. 5(d)]. Notably, the measurements obtained by such transducers were objective of a different study.

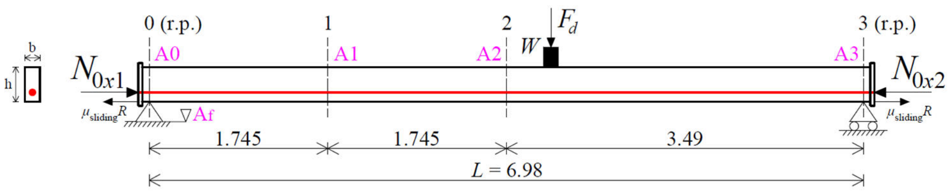

Fig. 4. The experimental set-up with the positions of hydraulic jack (W) and servo velocity seismometers (Af, A0, A1, A2 and A3). Units: m.

(a) (b) (c) (d)

Fig. 5. (a) Hinge support. (b) Roller support. (c) Hydraulic jack (W) on a rebar anchored near the midspan and seismometer A2 (Fig. 4). (d) Hydraulic hand pump to the floor before activation.

3.3. Free transverse vibrations

Free transverse vibrations were performed in a short term on the thin-walled box-girder following the application of $N_{0x,\text{aver}}$, in values of ≈ 117, 214, 332, 421, 501 and 598 kN, pulling the cables outward (Section 3.2). The girder was thus subjected to rotational boundary conditions due to the bending moments $N_{0x,\text{aver}}\, e$ at the RHS ends (Fig. 4). All seismometers (Af, A0, A1, A2 and A3) acquired the acceleration data at a sampling rate of 200 Hz, and with a Block Size (BS) of 131,072 samples. Vibration measurements were repeated thrice after that each post–tensioning force ($N_{0x,\text{aver}}$) was assigned. 18 experiments were totally executed. Particularly, free vibrations were induced pulling out a steel rebar, of 6 mm in diameter, welded at a distance not greater than 600 mm from the midspan (i = 2) both at right and left side (Fig. 4). Such procedure was feasible using a hydraulic oil jack W, of 120 mm in diameter, 170 mm in length, 100 kN in force capacity, and 118.5 N in mass, placed on the top of the girder and crossed by each rebar [Fig. 5(c)]. These latter were connected to the jack (W) at their higher end. Specifically, the jack pulled out every rebar from the girder counteracting its force on the girder itself. The jack was in turn actuated by a hydraulic hand pump, of 96.53 MPa in pressure capacity, positioned to the floor [Fig. 5(d)]. Therefore, the thin-walled box-girder with initial second-order curvature, due to the bending moments ($N_{0x,\mathrm{aver}}\, e$), total self-mass ($m_{\mathrm{tot,beam}} = m_{\mathrm{beam}} \times L = 5.0$ kN), and an axial end constraint, due to the stiffness of the cables [21, 22], was vibrated by small unbalanced forces caused by the unavoidable weld's breaking between rebar and member. In turn, weld's breaking was due to its lowest resistance (Fig. 4). Consequently, the value of the release forces (F_d) were of difficult estimations (Fig. 4) [17]. The vibrations were measured with respect to the RHS horizontal (strong) axis. The post–tensioning forces N_{0x1} and N_{0x2} were measured every second for a total of 200 seconds by a data acquisition unit using a different data logger. The average measurements of N_{0x1} and N_{0x2} for one repetition of vibration tests were listed in Table 2. The cables were never in contact with the surrounding RHS during vibrations (Fig. 4) unlike when the thin-walled box-girder was unloaded ($N_{0x,\mathrm{aver}}$=0). In this specific case, measurements were discarded. Notably, the eccentric post–tensioning force, when is assumed as externally applied, causes the yielding stress ($f_{yk} = 390$ MPa) of the most extreme fibres of midspan cross section at a value of $N_{0x,\mathrm{ULS},0.23} \approx 1{,}007$ kN (Fig. 4). $N_{0x,\mathrm{ULS},0.23}$ corresponds to ≈ 18.2% of the critical buckling load $N_{\mathrm{crE},1}$ or $N_{\mathrm{crE,shear},1} = 5{,}543$ kN.

3.4. Vibration frequencies

Figs. 6(a)–(b) show the acceleration from time-histories of the thin-walled box-girder, with corresponding Fast Fourier Transform (FFT) results, when the post–tensioning force $N_{0x,\mathrm{aver}} = 214$ kN (Fig. 4). BS = 65,536 samples. Particularly, Fig. 6(a) refers to the instrumented section (A1) at the quarter (i = 1), whilst Fig. 6(b) refers to the instrumented section (A2) at the midspan (i = 2). The raw signals (acceleration-time data) of each test repetition were imported into MATLAB [33] where a signal processing algorithm eliminated significant electrical noise [16]. The peak picking method was then adopted. Fundamental and second-mode frequencies were located at each peak of the FFT, as indicated in Figs. 6(a)–(b). Same procedure was done assuming a BS = 131,072 samples. A total of 72 of which were gathered, since each free vibration was repeated thrice, i.e., when the girder was subjected to each $N_{0x,\mathrm{aver}}$. Figs. 6(a)–(b) appertain both to one test repetition. Notably, the maximum $N_{0x,\mathrm{aver,max}}$ = 598 kN was ≈ 59% of the maximum allowable $N_{0x,\mathrm{ULS},0.23}$ ≈ 1,007 kN (Section 3.3).

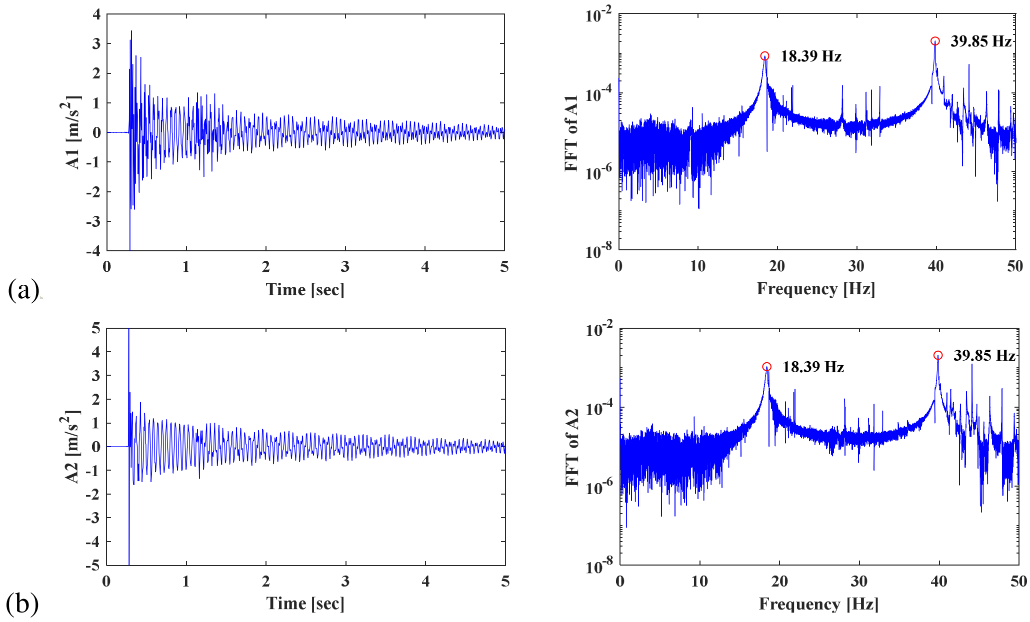

Fig. 6. Acceleration from time-histories and FFT results for $N_{0x,\mathrm{aver}}$=214 kN and BS=65,536 samples. Seismometers: (a) A1; (b) A2 (Fig. 4).

Seismometers A1 and A2 provided a slight increasing in fundamental frequency $f_{1,\mathrm{exp}}$ (almost constant) from 18.37 to 18.39 Hz into the initial increment in post–tensioning force ($N_{0x,\mathrm{aver}}$) which went from 117 to 214 kN. Subsequently, the girder was subjected to a significant softening effect: the frequency ($f_{1,\mathrm{exp}}$) underwent a prominent decrement of 0.93 Hz under an increment in $N_{0x,\mathrm{aver}}$ which went up to 598 kN. A maximum $f_{1,\mathrm{exp,max}}$ = 18.39 Hz and a minimum frequency $f_{1,\mathrm{exp,min}}$ = 17.46 Hz were finally measured within the experimental tendency. All frequencies ($f_{1,\mathrm{exp}}$) identified using seismometers A1 and A2, and a BS = 65,536 samples within the FFT of the 3 repetitions, were listed in Tables 2–3. The trend of $f_{1,\mathrm{exp}}$ was confirmed assuming a BS = 131,072 samples, i.e., increasing the accuracy in frequency estimations (200 Hz / 131,072 = 0.002 Hz). The only difference was the measurement $f_{1,\mathrm{exp}}$ = 17.91 Hz when the applied post–tensioning force $N_{0x,\mathrm{aver}}$ = 332 kN. Besides, seismometers A1 and A2 always furnished equal measurements ($f_{1,\mathrm{exp}}$) in relation to the same configuration of free vibration test (Section 3.3). Notably, the masses composed of load cell, threaded bars, circular and rectangular steel plate at one RHS end [Fig. 3(b)] were only ≈ 8.9% of the girder's total self-mass ($m_{\mathrm{tot,beam}}$ = 5.0 kN). Thus, conversely to what happened in the experiments of Noble et al. [14], it was avoided that such masses, lower than the total self-mass ($m_{tot,beam}$), affected the beam dynamics. Contrariwise, the second-mode frequencies were affected by the application of weak release forces (F_d) (Fig. 4). To obtain reliable second-mode frequency measurements through FFT, strong excitations are generally required to be induced during vibration testing [17]. Seismometer A1 was strategically located at a distance of 1.745 m from the midspan (at i = 1) since the latter is a nodal point for the second-mode vibration of a beam.

4. Interpretation of experimental results

4.1. Comparison with reference solutions

The fundamental frequencies ($f_{1,\mathrm{exp}}$) were firstly compared with Eqs. (1)–(2) and Eq. (4), in which, n = 1, whereas the corresponding critical buckling loads, $N_{\mathrm{crE},1}$ and $N_{\mathrm{crE,shear},1}$, were respectively assumed (Section 2). The comparisons were presented in Table 2, in which percentage errors were formulated by $\Delta = (f_1 - f_{1,\mathrm{exp}}) / f_{1,\mathrm{exp}}$. Specifically, $f_{\mathrm{E.\text{-}B.},1,II}$ decreased from ≈ 18.91 to 18.42 Hz into the increment in post–tensioning force ($N_{0x,\mathrm{aver}}$) went from ≈ 300 to 598 kN [Eq. (1)] corresponding to an average error Δ_{aver}=5.5%. Vice versa, $f_{\mathrm{shear},1,II}$ decreased from ≈ 18.80 to 18.32 Hz into the same range [Eq. (4)] corresponding to an average error Δ_{aver}=4.8%. The frequencies ($f_{1,\mathrm{exp}}$) followed the significant decreasing tendency of Eq. (1) and Eq. (4) and concurrent with the compression-softening theory. Therefore, the trend of frequencies ($f_{1,\mathrm{exp}}$) disagreed with findings and deductions of Noble et al. [14]. Yet, the differences between frequencies $f_{\mathrm{E.\text{-}B.},1,II}$ and $f_{\mathrm{shear},1,II}$ of ≈ 0.10 Hz (Table 2) were caused by the effect of shear deformation in Eq. (4). By contrast, the slight initial increment in $f_{1,\mathrm{exp}}$ of 0.02 Hz, i.e., into the range 117 kN $\leq N_{0x,\mathrm{aver}} \leq$ 214 kN, was not of the same rate as predicted by Eq. (1) and Eq. (4). Such trend occurred under a lower amount of second-order effects (≤ 4.0% of $N_{\mathrm{crE},1}$ or $N_{\mathrm{crE,shear},1}$), i.e., without a considerable softening effect along the thin-walled girder. Notably, the total self-mass per unit length (m_{tot}) considered the mass of hydraulic jack, W = 118.5 N [Fig. 5(c)], which was distributed along the length (L) of the member [$m_{\mathrm{tot}} = m_{\mathrm{beam}} + (W / L) = 0.7337$ kN/m]. W was equal to 2.4% of the total self-mass ($m_{\mathrm{tot,beam}}$=5.0 kN). Based also on published works and previous results [12, 17, 34, 35], masses of sensors or devices (affixed transversally) affect the fundamental frequency ($f_{1,\mathrm{exp}}$) of a simply supported beam when are greater than ≈ 0.3% of its total self-mass. This consideration is valid when strong excitations are induced by an impact or release force (F_d) because the precision in detection of frequency ($f_{1,\mathrm{exp}}$) is related to the complexity of signal's response, and to the proportion of vibrational response assigned to the fundamental mode [14, 15, 17]. FE analyses in Strand7 [36], discretizing the thin-walled box-girder into 20 elements, and accounting for total self-mass per unit length (m_{tot}), girder's axial deformations and curvatures, depending on post–tensioning ($N_{0x,\mathrm{aver}}$) and bending moments ($N_{0x,\mathrm{aver}}\ e$) at the RHS ends (Fig. 4), furnished the same frequencies $f_{\mathrm{E.\text{-}B.},1,II}$. The same values of frequencies $f_{\mathrm{shear},1,II}$ were also obtained including shear deformation in the FE model.

4.2. Comparison with the FE model proposed by Jaiswal including shear deformation

The frequencies ($f_{1,\mathrm{exp}}$) were secondly compared with the FE model proposed by Jaiswal [9] in which, the post–tensioning force ($N_{0x,\mathrm{aver}}$) is applied in the form of initial tension in the cables [17, 20]. Here $N_{0x,\mathrm{aver}}$ becomes an integral part of the thin-walled girder–cable system. As a result, $N_{0x,\mathrm{aver}}$ is not treated as a compressive force, as takes place in Eq. (1) and Eq. (4). Elastic material, geometric properties and self-masses per unit length m_{beam} and m_{tendon} (Table 1 and Section 3.1) were accounted for the corresponding FE model in Strand7 [36]. Transverse shear deformation was considered, whilst longitudinal vibrations, warping and rotary inertia were neglected [37]. Particularly, the thin-walled box-girder was discretized into 20 elements, whilst the 5 strands were modeled using a straight tendon (A_{tendon}) in turn discretized into 2 truss elements [Fig. 7(a)]. The tendon was aligned to the girder axis and only had common nodes at the RHS ends. Here, the eccentricity (e) was the distance of the tendon from the girder's center-line, as shown in Fig. 7(a). In such FE model for steel members with an eccentric unbonded tendon, only end nodes of beam and tendon are connected by rigid links [Fig. 7(a)]. The mass of the hydraulic jack, $W =$ 118.5 N [Fig. 5(c)], was first accounted as a distributed load [$m_{\mathrm{tot}} = m_{\mathrm{beam}} + (W/L)$]. Second, the jack was accounted as a concentrated mass (W) modeled as a short beam element and connected at the midspan [Fig. 7(a)]. To obtain the FE frequencies ($f_{\mathrm{E.\text{-}B.},1,II,\mathrm{FE}}$, $f_{\mathrm{shear},1,II,\mathrm{FE}}$, $f_{\mathrm{E.\text{-}B.},1,II,\mathrm{FE},W}$, $f_{\mathrm{shear},1,II,\mathrm{FE},W}$), a two-step approach was performed. The post–tensioning force ($N_{0x,\mathrm{aver}}$) was applied in the tendon, while axial deformations and second-order curvatures of the systems were gained. Artificial geometric imperfections were not included to prevent favoring instability modes. Then, the FE frequencies were evaluated for the corresponding new deformed configurations. Notably, the cross sectional area of strands (A_{tendon}) was assumed as unchanged after deformations. Vice versa, the deformed configurations related to the first-order FE frequencies ($f_{\text{E.-B.},1,I,\text{FE}}$, $f_{\text{shear},1,I,\text{FE}}$, $f_{\text{E.-B.},1,I,\text{FE},W}$, $f_{\text{shear},1,I,\text{FE},W}$) were only caused by the self-masses of girder, tendon and jack (W). Yet, an additional FE model was generated in which the tendon (A_{tendon}) was connected to the surrounding RHS by one rigid link at the midspan, as depicted in Fig. 7(b), thus simulating the presence of a deviator. Figs. 7(a)–(b) show the two fundamental flexural shapes $v^{(0)}$ of the thin-walled box-girder with concentrated mass (W) at the midspan: it is clearly visible that only the RHS ends are governed by the conservation of the planarity of the cross sections.

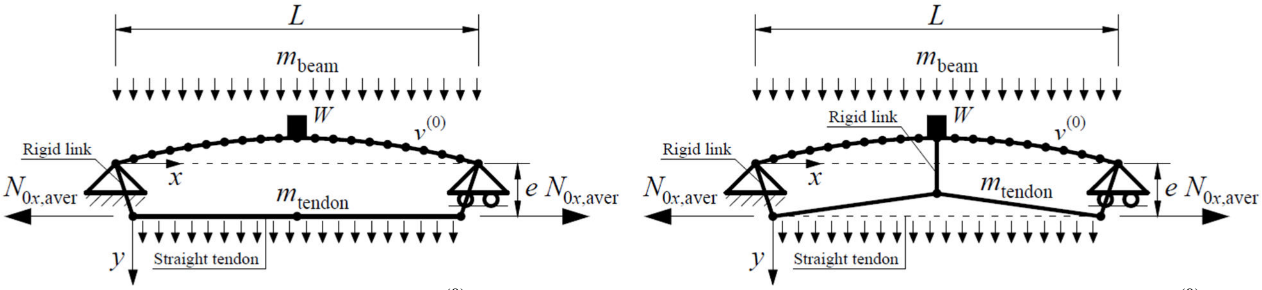

(a) Beam–tendon system [$v^{(0)}$] (b) Beam–tendon system with a deviator [$v^{(0)}$]

Fig. 7. FE model [9]. Fundamental flexural shapes $v^{(0)}$ according to the equivalent beam–tendon systems with mass W. The dashed lines represent the undeformed configurations.

The comparisons are listed in Table 3; percentage errors $\Delta = (f_{1,\text{FE}} - f_{1,\text{exp}}) / f_{1,\text{exp}}$. When the total self-mass per unit length (m_{tot}) was accounted, the FE frequencies $f_{\text{E.-B.},1,II,\text{FE}}$ decreased from ≈ 18.95 to 18.50 Hz into the increment ≈ $300 \leq N_{0x,\text{aver}} \leq 598$ kN, corresponding to an average error $\Delta_{\text{aver}} = 5.8\%$, whereas $f_{\text{shear},1,II,\text{FE}}$ decreased from ≈ 18.84 to 18.38 Hz into the same range, corresponding to an error $\Delta_{\text{aver}} = 5.2\%$. Conversely, when the jack was accounted as a mass (W), the FE frequencies $f_{\text{E.-B.},1,II,\text{FE},W}$ decreased from ≈ 18.73 to 18.29 Hz into ≈ $300 \leq N_{0x,\text{aver}} \leq 598$ kN, corresponding to an error $\Delta_{\text{aver}} = 4.6\%$, whereas $f_{\text{shear},1,II,\text{FE},W}$ decreased from ≈ 18.62 to 18.17 Hz, corresponding to an error $\Delta_{\text{aver}} = 4.0\%$. The experimental frequencies ($f_{1,\text{exp}}$) followed the decreasing tendency of the aforementioned FE frequencies (Table 3). Consequently, they disagreed with findings and deductions of Noble et al. [14]. Similarly to what predicted by the reference solutions (Section 4.1), the slight initial increment in frequency ($f_{1,\text{exp}}$) of 0.02 Hz was not of the same rate. Generally, the FE model, which included shear deformation, and accounted for the jack as a mass (W) at the midspan ($f_{\text{shear},1,II,\text{FE},W}$), better simulated the compression-softening effects. Table 3 also displays the trend of FE frequency ($f_{\text{shear},1,II,\text{FE},W,\text{D}}$) with the presence of a deviator [Fig. 7(b)]. In this configuration, the compression-softening effect is eliminated when the tendon is in contact with the surrounding thin-walled section: $f_{\text{shear},1,II,\text{FE},W,\text{D}}$ slightly decreased from 18.52 to 18.34 Hz into the increment $0 \leq N_{0x,\text{aver}} \leq 598$ kN. Notably, the FE model considered the slight influence of the bending moments at the pinned-end supports (Fig. 4), $M_{\mu} = \mu_{\text{sliding}} R \times h/2 = \mu_{\text{sliding}} \{ [(m_{\text{tot}} + m_{\text{tendon}}) \times L] / 2 \} \times h/2$, caused by the dynamic sliding friction between steel-on-steel. A frictional coefficient (μ_{sliding}) of 0.42, regarding the contact between dry steel-on-steel surfaces, was assumed [38].

The correlations summarized in Tables 2–3 confirmed the use of an accurate value of fundamental frequency ($f_{1,\text{exp}}$) as indicator for axial load estimation in steel beams, bridge cables and hangers [34, 39–42]. Yet, this work made certain such use for post–tensioning loss identification in thin-walled steel-girder-bridges with straight cables that are not in contact with the surrounding section [1, 43, 44]. In fact, second-order effects are not negligible when transverse vibrations are induced: a decrement in post–tensioning force ($N_{0x,\text{aver}}$) of 100 kN corresponds to an increment in $f_{1,\text{exp}}$ of ≈ 0.18 Hz. By contrast, when the cables are in contact with the section or draped with a deviator [43, 45, 46], its use as a parameter was made doubtful: a decrement in $N_{0x,\text{aver}}$ of 100 kN corresponds to an increment in $f_{1,\text{exp}}$ of 0.03 Hz. Regarding PC girder-bridges, the frequency ($f_{1,\text{exp}}$) was instead deduced to be a suitable indicator for flexural rigidity determination because the dynamics of a pre or post–tensioning force is experimentally negligible with a straight tendon [11, 47, 48] whilst is almost neglectable with a parabolic one [8, 12, 16].

4.3. Comparison with FE plate and shell modeling

FE plate and shell modeling was thirdly conducted to numerically compare the frequencies ($f_{1,\text{exp}}$). The spatial solution of the thin-walled steel-box-girder was discretized into a group of FE linked to each other in a certain manner. Since basic elements can be combined in different ways, FE analyses can solve problems of dynamics of thin-walled structures involving complicated geometries and/or boundary conditions [49, 50]. Elastic material, geometric properties, self-masses and unit weights (Table 1 and Section 3.1) were accounted in Strand7 [36]. The thin-walled box-girder was modeled using 276,860 plate/shell elements with a mesh size=5×5 mm^2. The 5 straight strands were discretized into 2 truss elements per each and fixed at the RHS ends according to the member design [Fig. 3(b)]. The plates for transducers (24,000 elements), internal stiffeners (6,948 elements) and plates at the RHS ends (3,846 elements) were also modeled using plate/shell elements with the same mesh size. The upper part of supports of 100 mm in width, 60 mm in height and 141 mm in length (13,536 elements), load cells (24,422 elements) and circular plates (12,211 elements) were instead modeled using brick elements with a mesh size=5×5×5 mm^3. The meshes between thin-walled girder, strands, plates and load cells were rigidly connected at the RHS ends. The seismometers A0, A1, A2 and A3 and the jack (W) [Fig. 5(c)] were modeled as short beams and connected along the girder according to the test layout (Fig. 4). Young's modulus of supports, load cells, circular plates, seismometers and jack (W) was assumed of 200 GPa, whilst υ = 0.25. Carriage-hinge external constraints, to have the pinned-end conditions, were arranged on a row of nodes at L (Fig. 4) whilst longitudinal vibrations, warping and rotary inertia were neglected. To obtain the FE frequencies ($f_{1,II,\mathrm{FE,P\&S}}$), the two-step procedure was conducted (Section 4.2). The post–tensioning force ($N_{0x,\mathrm{aver}}$) was applied in the strands and the axial deformation of the girder–tendon system was gained. Artificial geometric imperfections were not included. Subsequently, $f_{1,II,\mathrm{FE,P\&S}}$ were achieved. Yet, an additional FE model was created to simulate the contact between strands and surrounding RHS using one deviator, of 6 mm in thickness, at the midspan. 1,923 plate/shell elements with a mesh size=5×5 mm^2 were adopted ($\rho_{\mathrm{beam}} = 77.01$ kN/m^3; $E = 205.12$ GPa) [Fig. 8(b)]. In this case, the FE frequencies were labeled as $f_{1,II,\mathrm{FE,P\&S,D}}$. Fig. 8(a) and Fig. 8(c) respectively show the FE fundamental flexural shape of the thin-walled box-girder without and with deviator for $N_{0x,\mathrm{aver,max}} = 598$ kN.

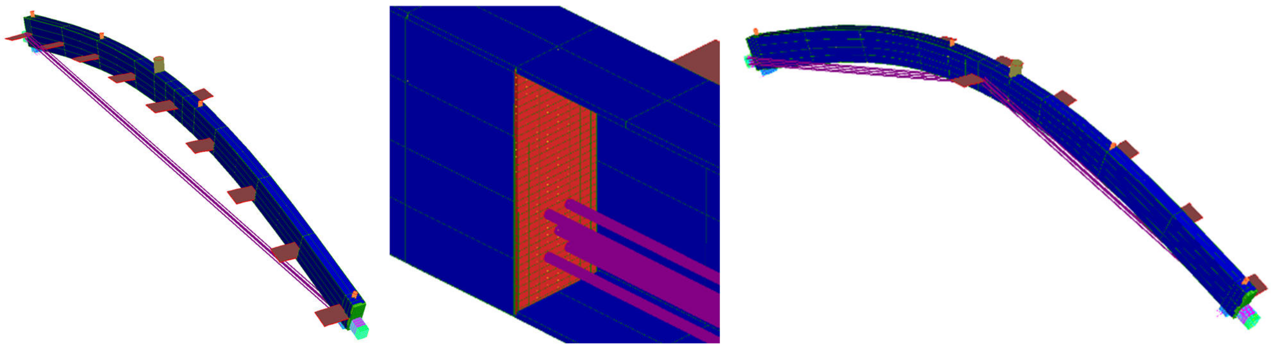

(a) (b) (c)

Fig. 8. FE plate/shell modeling in Strand7. Thin-walled box-girder (Fig. 4): (a) Fundamental flexural shape for $N_{0x,\mathrm{aver,max}}$=598 kN; (b) Deviator at the midspan; (c) Fundamental flexural shape with deviator ($N_{0x,\mathrm{aver,max}}$=598 kN).

Comparisons were reported in Table 2 [$\Delta = (f_{1,\mathrm{FE,P\&S}} - f_{1,\mathrm{exp}}) / f_{1,\mathrm{exp}}$]. $f_{1,II,\mathrm{FE,P\&S}}$ decreased from ≈ 18.61 to 18.14 Hz corresponding to an average error $\Delta_{\mathrm{aver}} = 3.8\%$. Therefore, the dynamics of the thin-walled box-girder was numerically well described since the experimental frequencies ($f_{1,\mathrm{exp}}$) properly followed the decreasing tendency of the compression-softening theory into the range ≈ $300 \leq N_{0x,\mathrm{aver}} \leq 598$ kN.

Conversely, $f_{1,II,\mathrm{FE,P\&S,D}}$ slightly decreased from 18.51 to 18.33 Hz into the increment $0 \le N_{0x,\mathrm{aver}} \le 598$ kN (Table 2). It was confirmed that the compression-softening effect is canceled when the cables are in contact with the surrounding thin-walled section (Section 4.2). Likewise, the FE plate and shell modeling always considered the dynamic sliding friction ($\mu_{\mathrm{sliding}} R$) at the girder's pinned-end supports (Fig. 4) because of the contact between dry steel-on-steel surfaces.

Table 2. Comparison between measured ($f_{1,\mathrm{exp}}$) and numerical fundamental frequencies from reference solutions [Eqs. (1), (2) and (4)] and FE plate and shell modeling. Seismometers A1 and A2 for BS = 65,536 samples (Fig. 4).

				Reference Solutions			FE Plate and Shell Modeling			
				Euler–Bernoulli	Shear		Shear		Shear with a Deviator	
				II–ord.	I–ord.	II–ord.	I–ord.	II–ord.	I–ord.	II–ord.
N_{0x1} (kN)	N_{0x2} (kN)	$N_{0x,\mathrm{aver}}$ (kN)	$f_{1,\mathrm{exp}}$ (Hz)	$f_{\mathrm{E.\text{-}B.},1,II}$ Eq. (1) (Hz)	$f_{\mathrm{shear},1,I}$ Eq. (2) (Hz)	$f_{\mathrm{shear},1,II}$ Eq. (4) (Hz)	$f_{1,I,\mathrm{FE,P\&S}}$ (Hz)	$f_{1,II,\mathrm{FE,P\&S}}$ (Hz)	$f_{1,I,\mathrm{FE,P\&S,D}}$ (Hz)	$f_{1,II,\mathrm{FE,P\&S,D}}$ (Hz)
–	–	0	–	19.50 –	19.39 –	– –	19.18 –	– –	18.51 –	– –
111	122	117	18.37 –	19.30 (5.1%)	19.39 (5.6%)	19.19 (4.5%)	19.18 (4.4%)	18.98 (3.3%)	18.51 –	18.47 –
205	222	214	18.39 –	19.12 (4.0%)	19.39 (5.4%)	19.01 (3.4%)	19.18 (4.3%)	18.82 (2.3%)	18.51 –	18.45 –
323	341	332	17.94 –	18.91 (5.4%)	19.39 (8.1%)	18.80 (4.8%)	19.18 (6.9%)	18.61 (3.7%)	18.51 –	18.41 –
410	432	421	17.78 –	18.75 (5.5%)	19.39 (9.1%)	18.64 (4.8%)	19.18 (7.9%)	18.45 (3.8%)	18.51 –	18.38 –
490	512	501	17.64 –	18.60 (5.4%)	19.39 (9.9%)	18.49 (4.8%)	19.18 (8.7%)	18.31 (3.8%)	18.51 –	18.36 –
586	610	598	17.46 –	18.42 (5.5%)	19.39 (11.1%)	18.32 (4.9%)	19.18 (9.9%)	18.14 (3.9%)	18.51 –	18.33 –
				$m_{\mathrm{tot}} = m_{\mathrm{beam}} + (W/L)$			m_{beam} and $W \rightarrow$ Mass W concentrated			

Table 3. Comparison between measured ($f_{1,\mathrm{exp}}$) and numerical fundamental frequencies from the FE model [9]. Seismometers A1 and A2 for BS = 65,536 samples (Fig. 4).

		FE Model proposed by Jaiswal									
		Euler–Bernoulli		Shear		Euler–Bernoulli		Shear		Shear with a Deviator	
		I–ord.	II–ord.	I–ord.	II–ord.	I–ord.	II–ord.	I–ord.	II–ord.	I–ord.	II–ord.
$N_{0x,\mathrm{aver}}$ (kN)	$f_{1,\mathrm{exp}}$ (Hz)	$f_{\mathrm{E.\text{-}B.},1,I,\mathrm{FE}}$ (Hz)	$f_{\mathrm{E.\text{-}B.},1,II,\mathrm{FE}}$ (Hz)	$f_{\mathrm{shear},1,I,\mathrm{FE}}$ (Hz)	$f_{\mathrm{shear},1,II,\mathrm{FE}}$ (Hz)	$f_{\mathrm{E.\text{-}B.},1,I,\mathrm{FE},W}$ (Hz)	$f_{\mathrm{E.\text{-}B.},1,II,\mathrm{FE},W}$ (Hz)	$f_{\mathrm{shear},1,I,\mathrm{FE},W}$ (Hz)	$f_{\mathrm{shear},1,II,\mathrm{FE},W}$ (Hz)	$f_{\mathrm{shear},1,I,\mathrm{FE},W,\mathrm{D}}$ (Hz)	$f_{\mathrm{shear},1,II,\mathrm{FE},W,\mathrm{D}}$ (Hz)
0	–	19.50 –	– –	19.39 –	– –	19.28 –	– –	19.17 –	– –	18.52 –	– –
117	18.37 –	19.50 (6.2%)	19.31 (5.1%)	19.39 (5.6%)	19.20 (4.5%)	19.28 (5.0%)	19.09 (3.9%)	19.17 (4.4%)	18.98 (3.3%)	18.52 –	18.49 –
214	18.39 –	19.50 (6.0%)	19.15 (4.1%)	19.39 (5.4%)	19.04 (3.5%)	19.28 (4.8%)	18.93 (2.9%)	19.17 (4.2%)	18.82 (2.3%)	18.52 –	18.46 –
332	17.94 –	19.50 (8.7%)	18.95 (5.6%)	19.39 (8.1%)	18.84 (5.0%)	19.28 (7.5%)	18.73 (4.4%)	19.17 (6.9%)	18.62 (3.8%)	18.52 –	18.42 –
421	17.78 –	19.50 (9.7%)	18.80 (5.7%)	19.39 (9.1%)	18.69 (5.1%)	19.28 (8.4%)	18.59 (4.6%)	19.17 (7.8%)	18.47 (3.9%)	18.52 –	18.40 –
501	17.64 –	19.50 (10.5%)	18.66 (5.8%)	19.39 (9.9%)	18.55 (5.2%)	19.28 (9.3%)	18.45 (4.6%)	19.17 (8.7%)	18.34 (4.0%)	18.52 –	18.37 –
598	17.46 –	19.50 (11.7%)	18.50 (6.0%)	19.39 (11.1%)	18.38 (5.3%)	19.28 (10.4%)	18.29 (4.8%)	19.17 (9.8%)	18.17 (4.1%)	18.52 –	18.34 –
		$m_{\mathrm{tot}} = m_{\mathrm{beam}} + (W/L)$				m_{beam} and $W \rightarrow$ Mass W concentrated					

5. Experiments performed by Noble et al.

5.1. Free transverse vibration of two thin-walled steel-box members post–tensioned by a concentric straight cable

In Noble et al. [14], the assumption that a post–tensioning force is whether or not dynamically equivalent to a compressive force was investigated (Section 1). To make sure that findings and deductions on our tests were effective (Section 4), numerical validations of the experiments performed by Noble et al. [14] were additionally executed. Specifically, the researchers carried out free transverse vibrations on two thin-walled steel members with RHS post–tensioned by a concentric straight cable. Beam 1 had b = 50 mm in width, h = 30 mm in height, and $t = t_{\mathrm{I}}$ = 3 mm in thickness, whereas Beam 2 had b = 120 mm, h = 60 mm, and $t = t_{\mathrm{I}}$ = 3 mm. Their total self-masses per unit length ($m_{\mathrm{tot}} = \rho_{\mathrm{beam}} \times A$) were 0.0343 and 0.0806 kN/m, respectively. The steel-box members were post–tensioned by a concentric steel "seven–wire" strand of 15.7 mm in diameter, whereas their material and geometric properties were summarized in Table 4. The self-mass per unit length of the strand ($m_{\mathrm{tendon}} = \rho_{\mathrm{tendon}} \times A_{\mathrm{tendon}}$) was instead 0.0114 kN/m. It was anchored with collets either side of two hydraulic jacks of 30 tons. in force capacity, and 222.7 N in mass per each (RCD307, Simplex). A load cell of 85 mm in diameter, 80 mm in length, 300 kN in force capacity, 1.5 mV/V in sensitivity, and 19.6 N in mass, was instead fixed at the extremities of the two jacks to measure the applied post–tensioning forces ($N_{0x,\mathrm{aver}}$) (KCM-300KNA, Tokyo Measuring Instruments Lab.). Moreover, a 200×150×20 mm^3 steel plate, of 77.01 kN/m^3 in unit weight, 200 GPa in Young's modulus, and 80 GPa in shear one, was positioned between each jack and the RHS end. Also, the members were pinned-end by steel knife-edge supports in a test rig, resulting in a clear length L (Table 4). One of the jacks was connected to a hydraulic hand pump to apply a post–tensioning force ($N_{0x,\mathrm{aver}}$) by pulling the strand outward. Thus, impact hammer testing were executed at incremental levels of $N_{0x,\mathrm{aver}}$ [Fig. 3 in Noble et al. [14]]. In Beam 1, the maximum induced second-order effects were ≈ 89% of its critical buckling load $N_{\mathrm{crE},1}$ or $N_{\mathrm{crE,shear},1}$ = 56 kN. Differently, in Beam 2, maximum second-order effects were ≈ 30% of its $N_{\mathrm{crE},1}$ or $N_{\mathrm{crE,shear},1}$ = 597 kN. The strand was only in contact at the edges, but not throughout the RHS length during vibrations. Therefore, the eccentricity (e) of $N_{0x,\mathrm{aver}}$ was theoretically zero (Fig. 1). Following execution of hammer testing, acceleration-time data, with respect to the specimens' horizontal axis, were acquired by an accelerometer of 6 g in mass, and 0.05 mV(m/s^2)$^{-1}$ in sensitivity, which was vertically arranged at the midspans (3200B4, Dytran Instruments) [Figs. 7 and 9 in Noble et al. [14]]. The FFT was then performed on the acceleration-time data to describe the signal in the frequency domain. And, peak picking method was used to identify the fundamental frequencies ($f_{1,\mathrm{exp}}$) (Section 3.4). The frequencies ($f_{1,\mathrm{exp}}$) were determined for each increment of post–tensioning force ($N_{0x,\mathrm{aver}}$) and each hammer test conducted [Figs. A1(b) and A1(d) in Noble et al. [14]]. More information on experiments and modal analyses are reported in Noble et al. [14]. The applied post–tensioning forces ($N_{0x,\mathrm{aver}}$) and average identified frequencies ($f_{1,\mathrm{exp}}$) were also listed in Table 5. For both specimens, a slight decreasing trend in frequency ($f_{1,\mathrm{exp}}$) was observed, which was not of the same rate as predicted by the Euler-Bernoulli theory [Eq. (1)]. In Beam 1, $f_{1,\mathrm{exp}}$ decreased from 27.77 to 24.77 Hz into the increment in post–tensioning force ($N_{0x,\mathrm{aver}}$) which went from 0 to 50 kN. Vice versa, in Beam 2, $f_{1,\mathrm{exp}}$ decreased from 75.35 to 72.85 Hz into an increment which went up to 180 kN. Regression lines were fitted to the data ($f_{1,\mathrm{exp}}$) and depicted in blue in Figs. 9(a)–(b). Accordingly, Noble et al. [14] concluded that a post–tensioning force is not dynamically equivalent to a compressive force. Strictly, the researchers deduced that the compression-softening theory is not applicable to prestressed structures. Based on our findings and deductions (Section 4), it is questionable that the frequencies ($f_{1,\mathrm{exp}}$) of their post–tensioned box members did not significantly follow the decreasing trend of the compression-softening theory [Figs. A1(b) and A1(d) in Noble et al. [14]].

Table 4. Noble et al. [14]. Properties of Beam 1 and Beam 2.

Property	Beam 1) RHS 50 × 30 × 3 mm^3	Beam 2) RHS 120 × 60 × 3 mm^3
I (mm^4)	6.1812 × 10^4	6.64092 × 10^5
A (mm^2)	444	1,044
A_w (mm^2)	144	324
Slenderness	127	59
k [Eq. (3)]	0.321	0.251
L (m)	1.5	
ρ_{beam} (kN/m^3)	77.20	
E (GPa)	205	
f_{yk} (MPa)	235	
G (GPa)	82	
υ	0.25	
A_{tendon} (mm^2)	149	
ρ_{tendon} (kN/m^3)	76.62	
E_{tendon} (GPa)	200	
σ_{uy} (MPa)	1,860	

5.2. Comparison with reference solutions

Following the numerical approaches described in Section 4, Noble et al. [14] 's fundamental frequencies ($f_{1,\mathrm{exp}}$) were firstly compared with Eq. (1) and Eq. (4) in which n = 1, whereas the critical buckling loads of Beams 1 and 2, $N_{\mathrm{crE},1}$ and $N_{\mathrm{crE,shear},1}$, were assumed (Section 2). Comparisons were presented in Figs. 9(a)–(b): the trends of frequencies $f_{\mathrm{E.\text{-}B.},1,II}$ were depicted in pink [Eq. (1)], whereas those of frequencies $f_{\mathrm{shear},1,II}$ were depicted in red with cross symbols [Eq. (4)]. In Beam 1, $f_{\mathrm{E.\text{-}B.},1,II}$ decreased from 42.04 to 13.32 Hz into the increment in post–tensioning force ($0 \leq N_{0x,\mathrm{aver}} \leq 50$ kN), whereas $f_{\mathrm{shear},1,II}$ decreased from 41.94 to 13.29 Hz [Fig. 9(a)]. In Beam 2, $f_{\mathrm{E.\text{-}B.},1,II}$ decreased from 89.87 to 75.11 Hz into the increment $0 \leq N_{0x,\mathrm{aver}} \leq 180$ kN, whereas $f_{\mathrm{shear},1,II}$ decreased from 88.64 to 74.09 Hz [Fig. 9(b)]. Therefore, the frequencies $f_{1,\mathrm{exp}}$, underlined by the blue regression lines, did not follow the significant decreasing tendency of the compression-softening theory of Eq. (1) and Eq. (4). The experimental behavior of the post–tensioned steel-box members was not well described confirming findings and deductions of Noble et al. [14]. The considerable softening effect, in terms of second-order effects, is particularly visible in Beam 1 (≈ 45% of its $N_{\mathrm{crE},1}$ or $N_{\mathrm{crE,shear},1}$). Indeed, the frequencies $f_{\mathrm{E.\text{-}B.},1,II}$ and $f_{\mathrm{shear},1,II}$ started to converge to the buckling loads ($N_{\mathrm{crE},1}$ and $N_{\mathrm{crE,shear},1}$) at a level of post–tensioning force ($N_{0x,\mathrm{aver}}$) of ≈ 25 kN. Notably also that, in Fig. 9(a), shear deformation is visibly negligible due to the high slenderness of Beam 1 equal to 127.

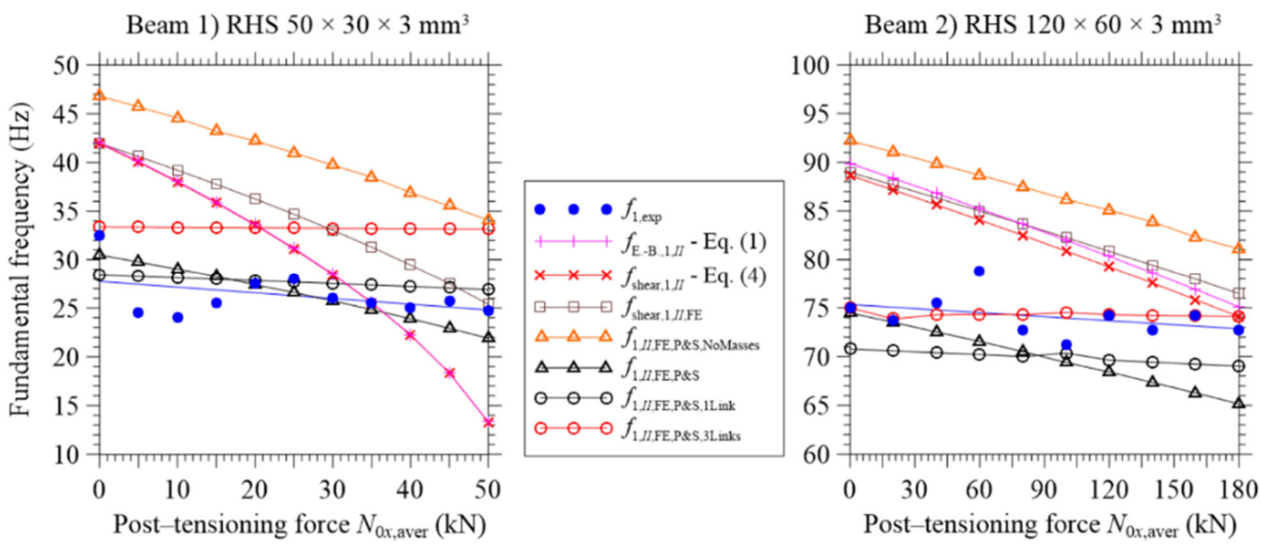

(a) Beam 1 (b) Beam 2

Fig. 9. Noble et al. [14]. Comparison between experimental ($f_{1,\mathrm{exp}}$) and numerical fundamental frequencies from reference solutions [Eqs. (1) and (4)] and FE models.

Table 5. Noble et al. [14]. Comparison between experimental ($f_{1,\mathrm{exp}}$) and numerical fundamental frequencies from FE plate and shell modeling.

Beam 1) RHS 50 × 30 × 3 mm^3					Beam 2) RHS 120 × 60 × 3 mm^3				
		Shear	Shear with 1 Rigid Link	Shear with 3 Rigid Links			Shear	Shear with 1 Rigid Link	Shear with 3 Rigid Links
		II–ord.	II–ord.	II–ord.			II–ord.	II–ord.	II–ord.
$N_{0x,\mathrm{aver}}$ (kN)	$f_{1,\mathrm{exp}}$ (Hz)	$f_{1,II,\mathrm{FE,P\&S}}$ (Hz)	$f_{1,II,\mathrm{FE,P\&S,1Link}}$ (Hz)	$f_{1,II,\mathrm{FE,P\&S,3Links}}$ (Hz)	$N_{0x,\mathrm{aver}}$ (kN)	$f_{1,\mathrm{exp}}$ (Hz)	$f_{1,II,\mathrm{FE,P\&S}}$ (Hz)	$f_{1,II,\mathrm{FE,P\&S,1Link}}$ (Hz)	$f_{1,II,\mathrm{FE,P\&S,3Links}}$ (Hz)
0	32.50 –	30.49 (-6.2%)	28.42 (-12.6%)	33.37 (2.7%)	0	75.00 –	74.48 (-0.7%)	70.78 (-5.6%)	75.00 (0.0%)
5	24.50 –	29.76 (21.5%)	28.27 (15.4%)	33.35 (36.1%)	20	73.75 –	73.52 (-0.3%)	70.59 (-4.3%)	73.87 (0.2%)
10	24.00 –	29.02 (20.9%)	28.13 (17.2%)	33.32 (38.8%)	40	75.50 –	72.52 (-3.9%)	70.39 (-6.8%)	74.29 (-1.6%)
15	25.50 –	28.26 (10.8%)	27.98 (9.7%)	33.30 (30.6%)	60	78.75 –	71.56 (-9.1%)	70.22 (-10.8%)	74.33 (-5.6%)
20	27.50 –	27.39 (-0.4%)	27.83 (1.2%)	33.28 (21.0%)	80	72.75 –	70.52 (-3.1%)	70.00 (-3.8%)	74.30 (2.1%)
25	28.00 –	26.59 (-5.0%)	27.68 (-1.1%)	33.26 (18.8%)	100	71.25 –	69.39 (-2.6%)	70.36 (-1.2%)	74.53 (4.6%)
30	26.00 –	25.74 (-1.0%)	27.53 (5.9%)	33.23 (27.8%)	120	74.25 –	68.42 (-7.9%)	69.64 (-6.2%)	74.30 (0.1%)
35	25.50 –	24.84 (-2.6%)	27.37 (7.3%)	33.21 (30.2%)	140	72.75 –	67.35 (-7.4%)	69.43 (-4.6%)	74.22 (2.0%)
40	25.00 –	23.90 (-4.4%)	27.22 (8.9%)	33.19 (32.8%)	160	74.25 –	66.27 (-10.7%)	69.22 (-6.8%)	74.17 (-0.1%)
45	25.75 –	22.92 (-11.0%)	27.06 (5.1%)	33.16 (28.8%)	180	72.75 –	65.16 (-10.4%)	69.02 (-5.1%)	74.10 (1.9%)
50	24.75 –	21.89 (-11.6%)	26.90 (8.7%)	33.14 (33.9%)					

5.3. Comparison with the FE model proposed by Jaiswal including shear deformation

Noble et al. [14] 's fundamental frequencies ($f_{1,\mathrm{exp}}$) were secondly compared with the FE model proposed by Jaiswal [9] which was created following the approaches described in Section 4.2. Elastic material, geometric properties and self-masses per unit length (m_{tot} and m_{tendon}) of the two post–tensioned box members (Table 4 and Section 5.1) were accounted for the corresponding FE models in Strand7 [36]. Particularly, the straight cable was aligned to the center-line of the members, and only connected to the end nodes of the RHS as shown in Fig. 10(a). Besides, Beams 1 and 2 were discretized into 20 elements, whilst cables were discretized into 2 truss elements [Fig. 10(a)]. To obtain the FE frequencies ($f_{\mathrm{shear},1,II,\mathrm{FE}}$), the two-step approach was performed. The post–tensioning force ($N_{0x,\mathrm{aver}}$) was applied in the cable and the axial static deformation of each system was achieved. Then, the FE frequencies ($f_{\mathrm{shear},1,II,\mathrm{FE}}$) were gained for the corresponding new deformed configurations. Notably, the cross sectional area of cables (A_{tendon}) was assumed as unchanged after deformations. Fig. 10(b) shows the FE fundamental flexural shape of Beam 2 for $N_{0x,\mathrm{aver,max}}$=180 kN [Fig. 9(b)]: it is clearly visible that the cable remains horizontal, thus only the ends of the member–cable system are governed by the conservation of the planarity of the cross sections.

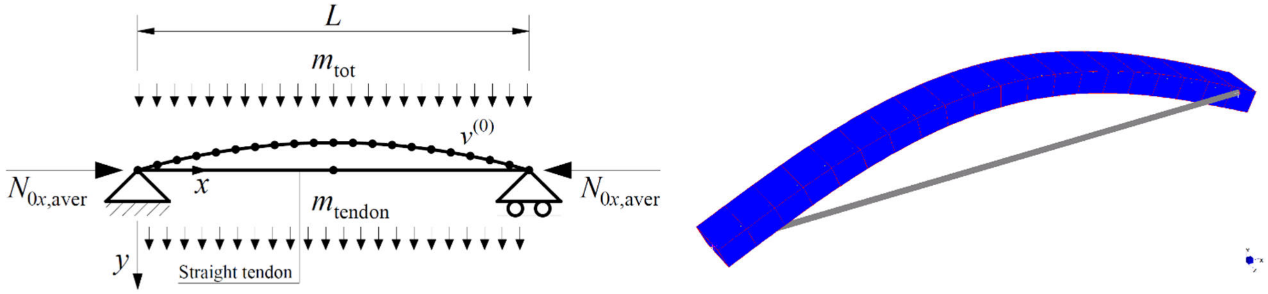

(a) Beam–cable system [$v^{(0)}$] (b) Shear ($f_{\mathrm{shear},1,II,\mathrm{FE}}$)

Fig. 10. Noble et al. [14]. FE model [9]. Fundamental flexural shapes: (a) $v^{(0)}$ according to the equivalent beam–cable system; (b) Beam 2 for $N_{0x,\mathrm{aver,max}}$=180 kN in Strand7.

The comparisons were presented in Figs. 9(a)–(b): the trends of FE frequencies $f_{\mathrm{shear},1,II,\mathrm{FE}}$ were depicted in brown. In Beam 1, $f_{\mathrm{shear},1,II,\mathrm{FE}}$ decreased from 41.96 to 25.39 Hz into the increment $0 \leq N_{0x,\mathrm{aver}} \leq 50$ kN [Fig. 9(a)]. Conversely, in Beam 2, $f_{\mathrm{shear},1,II,\mathrm{FE}}$ decreased from 88.96 to 76.47 Hz into $0 \leq N_{0x,\mathrm{aver}} \leq 180$ kN [Fig. 9(b)]. We see again that the frequencies $f_{1,\mathrm{exp}}$ did not follow the decreasing tendency of $f_{\mathrm{shear},1,II,\mathrm{FE}}$. Accordingly, the dynamics of the two post–tensioned members was not properly described. The softening effects were lower than those simulated by Eq. (1) and Eq. (4) because the cables increased the stiffness of each member–cable system. This behavior was extremely evident in Beam 1 having a high slenderness [Fig. 9(a)]. Notably, the FE models always considered the sliding friction ($\mu_{\mathrm{sliding}} R$) at the members' supports because of the contact between dry steel-on-steel surfaces (Section 4.2).

5.4. Comparison with FE plate and shell modeling

FE plate and shell modeling was thirdly conducted to numerically compare Noble et al. [14] 's frequencies ($f_{1,\mathrm{exp}}$). The FE approaches illustrated in Section 4.3 were adopted in Strand7 [36]. Each cable was discretized into 2 truss elements. Beams 1 and 2 were respectively modeled using 7,680 and 17,280 plate/shell elements corresponding to a mesh size of 5×6.25 mm^2. Instead, the two steel plates were modeled using 9,600 brick elements for a mesh size=5×5×5 mm^3. The meshes of thin-walled box members, cables and plates were rigidly connected at the RHS ends. Unit weights and elastic material properties were described in Table 4 and Section 5.1. Carriage-hinge external constraints were arranged on a row of nodes at L (Table 4). To obtain the FE frequencies ($f_{1,II,\mathrm{FE,P\&S,NoMasses}}$), the two-step procedure was similarly conducted. The post–tensioning force ($N_{0x,\text{aver}}$) was applied in the cable and the axial deformation of each system was gained. Subsequently, the FE frequencies ($f_{1,II,\text{FE,P\&S,NoMasses}}$) were achieved. In Beam 1, $f_{1,II,\text{FE,P\&S,NoMasses}}$ decreased from 46.82 to 34.07 Hz into the increment $0 \leq N_{0x,\text{aver}} \leq$ 50 kN [in orange in Fig. 9(a)]. Vice versa, in Beam 2, $f_{1,II,\text{FE,P\&S,NoMasses}}$ decreased from 92.20 to 81.11 Hz into $0 \leq N_{0x,\text{aver}} \leq 180$ kN [in orange in Fig. 9(b)]. The softening effects were affected by the steel plates at the RHS ends which increased the stiffness of each member–cable system.

The influence of load cells and hydraulic jacks was afterwards investigated: Bonopera et al. [11, 12] preliminarily declared that Noble et al. [14] 's frequencies ($f_{1,\text{exp}}$) were affected by such masses (Section 1). The load cells (KCM-300KNA), of 60 mm in width, 75 mm in height, 80 mm in length, modeled using 5,760 brick elements, for a mesh size=5×5×5 mm^3, were accounted with their proper mass (Section 5.1). Conversely, the hydraulic jacks (RCD307), of 100 mm in width, 90 mm in height, 220 mm in length, modeled using 31,680 brick elements, and with the same mesh size, were accounted with a lower mass. In fact, it was found that the jacks were arranged touching the floor at their mid length [Fig. 6.16. in Noble [51]]. Accordingly, their mass was hyphotetically reduced of 50% to decrease their dynamic contribution. Young's modulus of load cells and jacks was assumed of 200 GPa, whilst $\upsilon = 0.25$. The meshes between cables, plates, load cells and jacks were rigidly connected. The FE frequencies ($f_{1,II,\text{FE,P\&S}}$) were obtained using the two-step procedure. In Beam 1, $f_{1,II,\text{FE,P\&S}}$ decreased from 30.49 to 21.89 Hz into $0 \leq N_{0x,\text{aver}} \leq 50$ kN [in black with triangles in Fig. 9(a)]. Vice versa, in Beam 2, $f_{1,II,\text{FE,P\&S}}$ decreased from 74.48 to 65.16 Hz into $0 \leq N_{0x,\text{aver}} \leq 180$ kN [in black with triangles in Fig. 9(b)]. Subsequently, the contact between straight cable and surrounding RHS of the two box members was additionally simulated. First, it was simplified by one rigid link, which was used to connect cable and RHS upper part at their midspans. Second, it was simplified by three rigid links equidistant fastened along their length (L). In the first condition, for Beam 1, average percentage error $\Delta_{\text{aver,1Link}} = (f_{1,II,\text{FE,P\&S,1Link}} - f_{1,\text{exp}}) / f_{1,\text{exp}} = 6.0\%$ [Fig. 9(a)], whilst, for Beam 2, $\Delta_{\text{aver,1Link}} = -5.5\%$ [Fig. 9(b)]. In the second condition, for Beam 1, average error $\Delta_{\text{aver,3Links}} = (f_{1,II,\text{FE,P\&S,3Links}} - f_{1,\text{exp}}) / f_{1,\text{exp}} = 27.4\%$ [Fig. 9(a)], whilst, for Beam 2, $\Delta_{\text{aver,3Links}} = 0.4\%$ [Fig. 9(b)]. The errors (Δ) between experiments and FE plate and shell modeling for each $N_{0x,\text{aver}}$ were listed in Table 5. Figs. 11(a)–(f) show the FE fundamental flexural shapes of Beams 1 and 2 according to their maximum post–tensioning ($N_{0x,\mathrm{aver,max}}$). Based on the above correlations, it was confirmed that the mass at one end constraint, when is greater than the self-mass of the girder themselves, significantly affects the vibrational dynamics. Moreover, in Noble et al. [14], the cables probably touched the surrounding RHS causing stiffening effects which, in turn, falsified the decreasing tendencies of the compression-softening theory [Figs. A1(b) and A1(d)]. Similarly to what gathered by the FE analyses of our experiments (Sections 4.2 and 4.3), we deduced that the dynamics of a compressive force and that of a post–tensioning is different only when the cables are in contact with the surrounding beam's section. Likewise, the FE modeling always considered the sliding friction ($\mu_{\mathrm{sliding}} R$) at the members' supports because of the contact between dry steel-on-steel surfaces (Section 4.2).

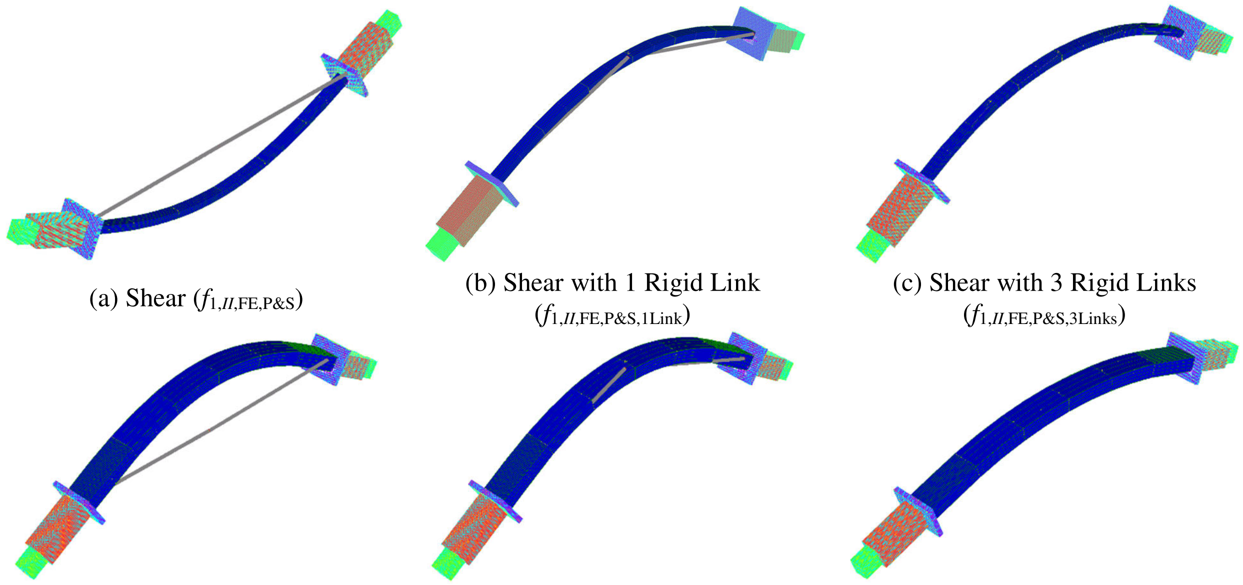

(a) Shear ($f_{1,II,\mathrm{FE,P\&S}}$)

(b) Shear with 1 Rigid Link ($f_{1,II,\mathrm{FE,P\&S,1Link}}$)

(c) Shear with 3 Rigid Links ($f_{1,II,\mathrm{FE,P\&S,3Links}}$)

(d) Shear ($f_{1,II,\mathrm{FE,P\&S}}$)

(e) Shear with 1 Rigid Link ($f_{1,II,\mathrm{FE,P\&S,1Link}}$)

(f) Shear with 3 Rigid Links ($f_{1,II,\mathrm{FE,P\&S,3Links}}$)

Fig. 11. Noble et al. [14]. FE plate/shell modeling in Strand7. Fundamental flexural shapes: (a–c) Beam 1 for $N_{0x,\mathrm{aver,max}}$=50 kN; (d–f) Beam 2 for $N_{0x,\mathrm{aver,max}}$=180 kN.

6. Relationship between free transverse vibration and critical buckling

The effect of the location of straight cables on the relationship between free transverse vibrations and critical buckling including shear deformation was discussed. In order to observe the evolution of fundamental frequency in more detail, Fig. 12 and Fig. 13 compare the stability of thin-walled member–cable systems [Fig. 7(a)] with that of the same girders when externally axially loaded (Fig. 1). In the second case, the stability is determined by the critical force ($N_{0x,\mathrm{aver}}$) for which the fundamental frequency drops to zero [23]. For our thin-walled steel-box-girder (Fig. 2), the stability was numerically studied since it was not possible to over post–tensioning the beam in the experimental set-up (Fig. 4). Fig. 12

demonstrates that increasing the post–tensioning force ($N_{0x,\mathrm{aver}}$), the FE frequency $f_{\mathrm{shear},1,II,\mathrm{FE},W}$ considerably reduces up to $N_{0x,\mathrm{aver}}$ of ≈ 1,000 kN, corresponding to the eccentric post–tensioning force ($N_{0x,\mathrm{ULS},0.23}$) which causes the yielding stress of the most extreme fibres of midspan cross section. Subsequently, $f_{\mathrm{shear},1,II,\mathrm{FE},W}$ increases because of the stiffening effect due to the cables' eccentricity (e / h = 0.23), i.e., when the thin-walled girder is subjected to higher bending moments at the RHS ends ($N_{0x,\mathrm{aver}}$ e) and second-order curvatures [21, 22]. Nonetheless, the eccentric post–tensioning force ($N_{0x,\mathrm{pl},0.23}$), which causes the plasticity of the cross section, is equal to 1,484 kN. Conversely, when the eccentricity of cables is large (e / h = 0.74), the stiffening effect generally prevails and the vibration tendon mode is dominant. In this case, $N_{0x,\mathrm{ULS},0.74}$ and $N_{0x,\mathrm{pl},0.74}$ become respectively equal to 502 and 758 kN (Fig. 12). Yet, when the corresponding initial second-order curvatures of the girder are not imposed as deformed configurations (Section 4.2), $f_{\mathrm{shear},1,II,\mathrm{FE},W}$ follows the decreasing trend of the compression-softening theory which, in turn, does not depend on cables' eccentricity (e), as occurred using FE plate and shell modeling ($f_{1,II,\mathrm{FE,P\&S}}$), Eq. (1) or Eq. (4). Specifically, the course of $f_{\mathrm{shear},1,II,\mathrm{FE},W}$ converges to a critical buckling load of 5,890 kN, which is higher than $N_{\mathrm{crE},1}$ or $N_{\mathrm{crE,shear},1}$ = 5,543 kN (Fig. 12), because of a stiffening effect due to the formation of rotational elastic conditions in the cables at the RHS ends. Notably, post–tensioned thin-walled steel-girder-bridges draped with a deviator [43, 45, 46] almost never experience critical buckling phenomena [Fig. 7(b)] as commonly happened in PC girder-bridges [17].

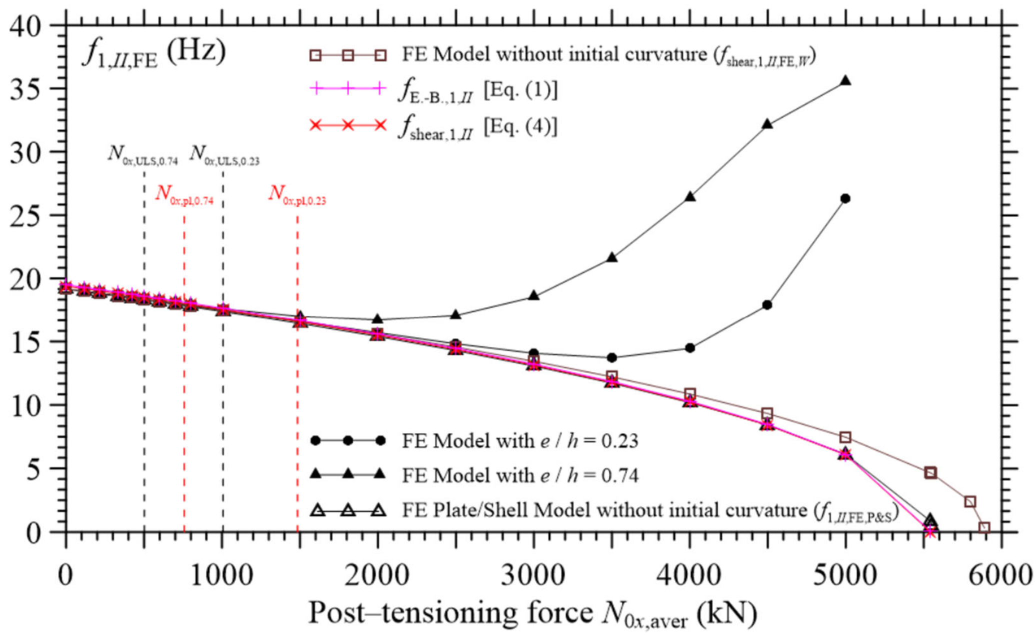

Fig. 12. Thin-walled member (Fig. 4). Effect of the post–tensioning force ($N_{0x,\mathrm{aver}}$) on the fundamental frequency.

Fig. 13 shows the trend of $f_{\mathrm{shear},1,II,\mathrm{FE}}$ of the thin-walled steel-girder-bridge with unbonded cables utilized in the numerical study presented by Bai-jian et al. [1]. Likewise, increasing the post–tensioning force (N_{0x}) up to the critical buckling of the girder–cable system of 3,845 kN, $f_{\mathrm{shear},1,II,\mathrm{FE}}$ reduces the negative slope of its softening branch according to the cables' eccentricity (e), i.e., from small ($e/h = 0.12$) to medium ($e/h = 0.28$). The eccentric $N_{0x,\mathrm{ULS},0.12}$ and $N_{0x,\mathrm{pl},0.12}$ are respectively equal to 433 and 669 kN when $e/h = 0.12$. Vice versa, $N_{0x,\mathrm{ULS},0.28}$ and $N_{0x,\mathrm{pl},0.28}$ become 314 and 483 kN when $e/h = 0.28$ (Fig. 13). Thin-walled member–cable systems with an eccentrically straight tendon have two sets of fundamental vibrational modes, i.e., beam-dominated and tendon-dominated modes. Particularly, their dynamic interaction depends not only on the magnitude of post–tensioning force (N_{0x}) but also on the location of the tendon that induces an initial second-order curvature along the member. We can state that the vibration beam mode follows the compression-softening theory when tendon's eccentricity (e) is zero, and it is almost always dominant when the yielding stress under post–tensioning (N_{0x}) is not reached.

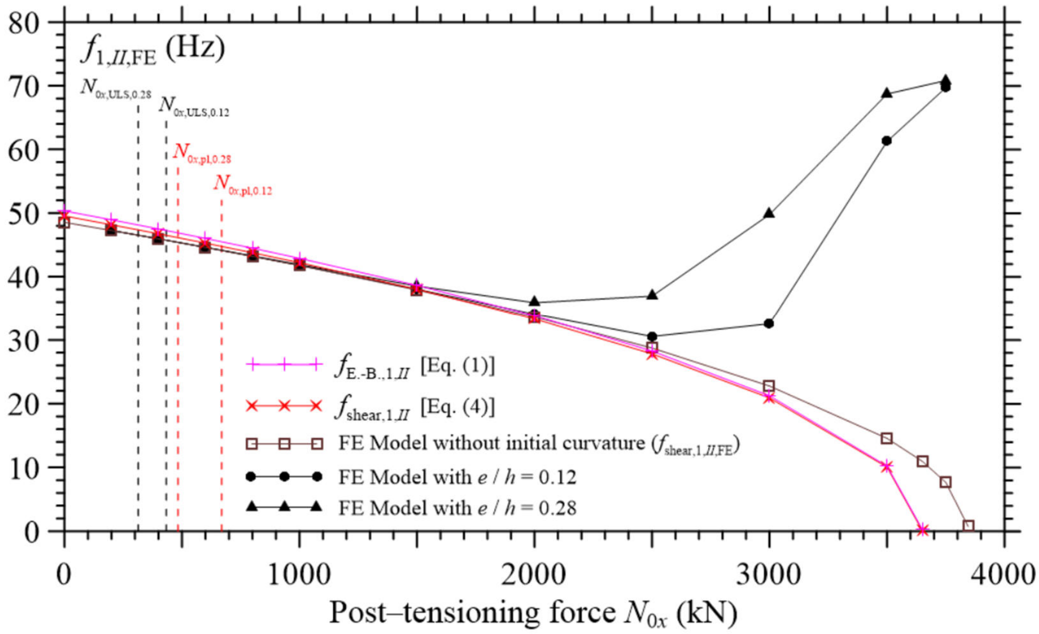

Fig. 13. Thin-walled girder-bridge [1]. Effect of the post–tensioning force (N_{0x}) on the fundamental frequency.

7. Conclusions

The effect of pre and post–tensioning forces on the beam dynamics is object of a significant discrepancy. To solve this conflict, firstly, free transverse vibrations were induced to a post–tensioned thin-walled steel-box-girder in larger scale and with eccentric straight cables. Secondly, to finally investigate the validity of the compression-softening theory in prestressed beams, the experiments performed by Noble et al. [14] were analyzed. Within the limitations of this research and the results thoroughly validated using the bench-top experiment (Fig. 4), one proposed formula based on Timoshenko beam model [Eq. (4)], and two high-fidelity FE models including shear deformation, the following conclusions are reported:

1. The experimental dynamics were appropriately simulated using the FE model proposed by Jaiswal [9] and that based on plate and shell elements. In thin-walled member–cable systems, both modeling apply the effective post–tensioning force ($N_{0x,\text{aver}}$) in the form of initial tension in the cables whilst neglect the corresponding second-order curvature. Accordingly, the fundamental frequency ($f_{1,\text{exp}}$) of thin-walled steel members is not influenced by the beam's camber (initial curvature) until the yielding stress (f_{yk}) under post–tensioning ($N_{0x,\text{aver}}$) is reached.
2. Conversely to what concluded by Noble et al. [14, 15], the dynamic effect of a compressive force and that of a post–tensioning phenomenologically differ only when the cables are in contact with the surrounding beam's section [Fig. 7(b)]. Depending on this characteristic, the dynamics of all forms of pre and post–tensioned members is described by compression-softening effect.
3. Similarly to what deduced for PC girder-bridges [7, 19, 20], the fundamental frequency ($f_{1,\text{exp}}$) as parameter for post–tensioning loss identification is made doubtful in thin-walled steel-girder-bridges when the cables touch the surrounding section or are draped with a deviator [Fig. 8(b)].
4. When the beam's cambers (initial curvatures) are considered as deformed configurations within the FE modeling, thin-walled member–cable systems have two sets of fundamental vibrational modes (Figs. 12–13). By increasing the post–tensioning force ($N_{0x,\text{aver}}$) beyond the value causing the yielding stress of the most extreme fibres of cross section (f_{yk}), a stiffening effect occurs. This consequence depends on the straight tendon's eccentricity (e): when it is small ($e\,/\,h = 0.12 \sim 0.23$) the softening effect is prevalent than the stiffening one and the vibration beam mode is dominant. Vice versa, when the eccentricity is large ($e\,/\,h = 0.44 \sim 0.74$) the stiffening effect prevails and the vibration tendon mode is dominant (Figs. 12–13).

CRediT authorship contribution statement

M. Bonopera: Formulation and evolution of overarching research goals and aims, Funding acquisition, Methodology, Numerical validation of theory using commercial software, Substantial contribution to conception, Writing - original draft. **K.-C. Chang**: Methodology, Substantial contribution to acquisition of data results, Substantial contribution to replication of results. **N. Tullini**: Funding acquisition, Ideas, Methodology, Substantial contribution to acquisition of data results, Substantial contribution to conception, Writing - review & editing.

Declaration of competing interest

The authors declare that they have no known competing financial interests or personal relationships that could have appeared to influence the work reported in this paper.

Acknowledgments

The tests were executed at the NCREE and funded by the National Applied Research Laboratories Project of Taiwan [NCREE–06107A1700]. M.B. acknowledges the funding provided by the Ministry Of Science and Technology (MOST) of Taiwan under the framework of the project "Recruitment of Visiting Science and Technology Personnel" [MOST 109–2811–E–492–500]. N.T. acknowledges the financial support of the "Research Program FAR 2022" provided by the University of Ferrara. Special gratitude is extended to the laboratory technicians of the NCREE, who furnished assistance to the authors, and to Dr. Darragh Noble of the University of Dublin for the help in providing several information about his experiments.

Nomenclature

A : cross sectional area of the thin-walled Rectangular Hollow Section (RHS)
Af, A0, A1, A2, A3 : servo velocity seismometers
A_{tendon} : cross sectional area of straight tendon
A_w : cross sectional area of the web of a thin-walled RHS
b : internal width of a thin-walled RHS
e : eccentricity of straight tendon
E : Young's modulus of the thin-walled member
E_{tendon} : Young's modulus of straight tendon
$f_{1,I,\mathrm{FE,P\&S}}$: first-order fundamental frequency based on FE plate/shell modeling
$f_{1,I,\mathrm{FE,P\&S,D}}$: first-order fundamental frequency with a deviator based on FE plate/shell modeling
$f_{1,II,\mathrm{FE,P\&S}}$: second-order fundamental frequency based on FE plate/shell modeling
$f_{1,II,\mathrm{FE,P\&S,1Link}}$: second-order fundamental frequency with 1 rigid link based on FE plate/shell modeling
$f_{1,II,\mathrm{FE,P\&S,3Links}}$: second-order fundamental frequency with 3 rigid links based on FE plate/shell modeling
$f_{1,II,\mathrm{FE,P\&S,D}}$: second-order fundamental frequency with a deviator based on FE plate/shell modeling
$f_{1,II,\mathrm{FE,P\&S,NoMasses}}$: second-order fundamental frequency without masses at the RHS ends based on FE plate/shell modeling
$f_{1,\mathrm{exp}}$: experimental fundamental frequency
$f_{1,\mathrm{exp,max}}$: experimental maximum fundamental frequency
$f_{1,\mathrm{exp,min}}$: experimental minimum fundamental frequency
$f_{\mathrm{E.\text{-}B.},1,I}$: first-order fundamental frequency based on Euler-Bernoulli model

$f_{\text{E.-B.},1,I,\text{FE}}$: first-order fundamental frequency based on FE model
$f_{\text{E.-B.},1,I,\text{FE},W}$: first-order fundamental frequency with mass W based on FE model
$f_{\text{E.-B.},1,II}$: second-order fundamental frequency based on Euler-Bernoulli model
$f_{\text{E.-B.},1,II,\text{FE}}$: second-order fundamental frequency based on FE model
$f_{\text{E.-B.},1,II,\text{FE},W}$: second-order fundamental frequency with mass W based on FE model
$f_{\text{E.-B.},n,II}$: second-order nth natural frequency based on Euler-Bernoulli model
$f_{\text{shear},1,I}$: first-order fundamental frequency based on shear model
$f_{\text{shear},1,I,\text{FE}}$: first-order fundamental frequency based on FE model including shear deformation
$f_{\text{shear},1,I,\text{FE},W}$: first-order fundamental frequency with mass W based on FE model including shear deformation
$f_{\text{shear},1,I,\text{FE},W,\text{D}}$: first-order fundamental frequency with mass W and deviator based on FE model including shear deformation
$f_{\text{shear},1,II}$: second-order fundamental frequency based on shear model
$f_{\text{shear},1,II,\text{FE}}$: second-order fundamental frequency based on FE model including shear deformation
$f_{\text{shear},1,II,\text{FE},W}$: second-order fundamental frequency with mass W based on FE model including shear deformation
$f_{\text{shear},1,II,\text{FE},W,\text{D}}$: second-order fundamental frequency with mass W and deviator based on FE model including shear deformation
$f_{\text{shear},n,I}$: first-order nth natural frequency based on shear model
$f_{\text{shear},n,II}$: second-order nth natural frequency based on shear model
F_d : release force of transverse vibration tests
f_{yk} : yielding stress of the thin-walled member
g : gravitational acceleration
G : shear modulus of the thin-walled member
h : height of a thin-walled RHS
i : measurement cross section along the thin-walled member
I : cross sectional second moment of the area of the thin-walled member
k : shear coefficient for a generic thin-walled RHS
L : length of the thin-walled member
m : coefficient considering the shear stresses throughout the cross sectional area of a thin-walled RHS
m_{beam} : thin-walled member's self-mass per unit length
m_{tendon} : straight tendon's self-mass per unit length
m_{tot} : thin-walled member's total self-mass per unit length corresponding to $m_{\text{beam}} + W/L$.
$m_{\text{tot,beam}}$: thin-walled member's total self-mass
M_μ : bending moments at the supports caused by sliding friction between steel-on-steel
n : vibration beam mode
N_{0x} : mean post–tensioning force
N_{0x1} : applied post–tensioning force at the left RHS end
N_{0x2} : applied post–tensioning force at the right RHS end
$N_{0x,\text{aver}}$: mean applied post–tensioning force
$N_{0x,\text{aver,max}}$: maximum mean applied post–tensioning force
$N_{0x,\text{pl},0.12}$: mean post–tensioning force causing the plasticity of cross section when $e / h = 0.12$
$N_{0x,\text{pl},0.23}$: mean post–tensioning force causing the plasticity of cross section when $e / h = 0.23$
$N_{0x,\text{pl},0.28}$: mean post–tensioning force causing the plasticity of cross section when $e / h = 0.28$
$N_{0x,\text{pl},0.74}$: mean post–tensioning force causing the plasticity of cross section when $e / h = 0.74$
$N_{0x,\text{ULS},0.12}$: mean post–tensioning force causing the yielding stress of the most extreme fibres of cross section when $e / h = 0.12$
$N_{0x,\text{ULS},0.23}$: mean post–tensioning force causing the yielding stress of the most extreme fibres of cross section when $e / h = 0.23$
$N_{0x,\text{ULS},0.28}$: mean post–tensioning force causing the yielding stress of the most extreme fibres of cross section when $e / h = 0.28$
$N_{0x,\text{ULS},0.74}$: mean post–tensioning force causing the yielding stress of the most extreme fibres of cross section when $e / h = 0.74$
$N_{\text{crE},1}$: Euler buckling load

$N_{\mathrm{crE},n}$: nth critical buckling load
$N_{\mathrm{crE,shear},1}$: first critical buckling load including shear deformation
$N_{\mathrm{crE,shear},n}$: nth critical buckling load including shear deformation
r : radius of inertia of the thin-walled RHS
t : thickness of the web of a thin-walled RHS
t_{I} : thickness of the flanges of a thin-walled RHS
υ : Poisson's ratio of the thin-walled member
$v^{(0)}$: flexural shape of the fundamental frequency
W : mass of hydraulic oil jack
μ_{sliding} : frictional coefficient regarding the contact between steel-on-steel surfaces at the supports
ρ_{beam} : unit weight of the thin-walled member
ρ_{tendon} : unit weight of straight tendon
$\sigma_{\mathrm{tendon,max}}$: maximum tensile strength reached in the straight tendon
σ_{uy} : yielding stress of straight tendon

References

1. T. Bai-jian, W. Fei, C. Song, Effect of prestress force on natural bending frequency of external prestressed steel beams, *Open Civ. Eng. J.* **12** (2018) 62–70.
2. B.Z. Gan, S.P. Chiew, Y. Lu, T.C. Fung, The effect of prestressing force on natural frequencies of concrete beams - A numerical validation of existing experiments by modelling shrinkage crack closure, *J. Sound Vib.* **455** (2019) 20–31.
3. J.A. De Lana, P.A.A.M. Júnior, C.A. Magalhães, A.L.M.A. Magalhães, A.C. De Andrade Junior, M.S. De Barros Ribeiro, Behavior study of prestressed concrete wind-turbine tower in circular cross-section, *Eng. Struct.* **227** (2021) 111403.
4. M.E.M. Kambal, Y. Jia, Theoretical and experimental study on flexural behavior of prestressed steel plate girders, *J. Constr. Steel Res.* **142** (2018) 5–16.
5. C. Rebelo, M. Veljkovic, L.S. Da Silva, R. Simões, J. Henriques, Structural monitoring of a wind turbine steel tower - Part I: System description and calibration, *Wind Struct. Int. J.* **15** (4) (2012) 285–299.
6. Y. Yang, Y. Zhu, L.L. Wang, B.Y. Jia, R. Jin, Structural damage identification of bridges from passing test vehicles, *Sensors* **18** (2018) 1–23.
7. M. Bonopera, K.C. Chang, Z.K. Lee, State-of-the-art review on determining prestress losses in prestressed concrete girders, *Appl. Sci.* **10** (20) (2020).
8. E. Hamed, Y. Frostig, Natural frequencies of bonded and unbonded pre–stressed beams pre–stress force effects, *J. Sound Vib.* **295** (1–2) (2006) 28–39.

9. O.R. Jaiswal, Effect of prestressing on the first flexural natural frequency of beams, *Struct. Eng. Mech.* **28** (5) (2008) 515–524.
10. M.P. Limongelli, D. Siegert, E. Merliot, J. Waeytens, F. Bourquin, R. Vidal, V. Le Corvec, I. Gueguen, L.M. Cottineau, Damage detection in a post tensioned concrete beam – Experimental investigation, *Eng. Struct.* **128** (2016) 15–25.
11. M. Bonopera, K.C. Chang, C.C. Chen, Y.C. Sung, N. Tullini, Prestress force effect on fundamental frequency and deflection shape of PCI beams, *Struct. Eng. Mech.* **67** (3) (2018).
12. M. Bonopera, K.C. Chang, C.C. Chen, Y.C. Sung, N. Tullini, Experimental study on the fundamental frequency of prestressed concrete bridge beams with parabolic unbonded tendons, *J. Sound Vib.* **455** (2019) 150–160.
13. M.A. Pisani, M.P. Limongelli, P.F. Giordano, M. Palermo, On the effectiveness of vibration-based monitoring for integrity management of prestressed structures, *Infrastructures* **6** (12) (2021).
14. D. Noble, M. Nogal, A. O'Connor, V. Pakrashi, Dynamic impact testing on post–tensioned steel rectangular hollow sections; An investigation into the "compression–softening" effect, *J. Sound Vib.* **355** (2015) 246–263.
15. D. Noble, M. Nogal, A. O'Connor, V. Pakrashi, The effect of prestress force magnitude and eccentricity on the natural bending frequencies of uncracked prestressed concrete beams, *J. Sound Vib.* **365** (2016) 22–44.
16. M. Bonopera, K.C. Chang, T.K. Lin, N. Tullini, Influence of prestressing on the behavior of uncracked concrete beams with a parabolic bonded tendon, *Struct. Eng. Mech.* **77** (1) (2021) 1–17.
17. M. Bonopera, W.C. Liao, W. Perceka, Experimental–theoretical investigation of the short-term vibration response of uncracked prestressed concrete members under long-age conditions, *Structures* **35** (2022) 260–273.
18. M. Bonopera, K.C. Chang, C.C. Chen, Z.K. Lee, N. Tullini, Axial load detection in compressed steel beams using FBG–DSM sensors, *Smart Struct. Syst.* **21** (1) (2018) 53–64.

19. M. Bonopera, K.C. Chang, C.C. Chen, Y.C. Sung, N. Tullini, Feasibility study of prestress force prediction for concrete beams using second–order deflections, *Int. J. Struct. Stab. Dy.* **18** (10) (2018) 1–19.
20. M. Bonopera, K.C. Chang, Novel method for identifying residual prestress force in simply supported concrete girder-bridges, *Adv. Struct. Eng.* **24** (14) (2021) 3238–3251.
21. S. Ilanko, The vibration behaviour of initially imperfect simply supported beams subject to axial loading, *J. Sound Vib.* **142** (2) (1990) 355–359.
22. A. Carpinteri, R. Malvano, A. Manuello, G. Piana, Fundamental frequency evolution in slender beams subjected to imposed axial displacements, *J. Sound Vib.* **333** (2014) 2390–2403.
23. Z.P. Bažant, L. Cedolin, *Stability of Structures: Elastic, Inelastic, Fracture and Damage Theories* (World Scientific, 2010).
24. S.M. Han, H. Benaroya, T. Wei, Dynamics of transversely vibrating beams using four engineering theories, *J. Sound Vib.* **225** (5) (1999) 935–988.
25. N. Challamel, On the comparison of Timoshenko and shear models in beam dynamics, *J. Eng. Mech.* **132** (10) (2006) 1141–1145.
26. F. Minghini, N. Tullini, F. Laudiero, Vibration analysis with second-order effects of pultruded FRP frames using locking-free elements, *Thin-Walled Struct.* **47** (2) (2009) 136–150.
27. F. Minghini, N. Tullini, F. Laudiero, Elastic buckling analysis of pultruded FRP portal frames having semi-rigid connections, *Eng. Struct.* **31** (2) (2009) 292–299.
28. K.K. Raju, G.V. Rao, Free vibration behavior of prestressed beams, *J. Struct. Eng.* **112** (2) (1986) 433–437.
29. S.S. Rao, *Continuous Systems*, In *Mechanical Vibrations*; S.S. Rao; 5th Edition, Prentice Hall, Upper Saddle River, NJ, USA (2011) 699–768.
30. V. Ondra, B. Titurus, Theoretical and experimental free vibration analysis of a beam-tendon system with an eccentrically placed tendon, *Thin-Walled Struct.* **144** (2019) 106347.
31. G.R. Cowper, The shear coefficient in Timoshenko's beam theory, *J. Appl. Mech.* **33** (2) (1966) 335–340.

32. ASTM E8/E8M–16a, Standard Test Methods for Tension Testing of Metallic Materials, American Society for Testing & Materials International, West Conshohocken, PA (2016).
33. MATLAB, MATLAB documentation, Introduction to GUIDE, The Mathworks, Inc., 2021a, http://www.mathworks.com/help/matlab/creating_guis/introduction-to-guide.html.
34. K. Maes, J. Peeters, E. Reynders, G. Lombaert, G. De Roeck, Identification of axial forces in beam members by local vibration measurements, *J. Sound Vib.* **332** (21) (2013) 5417–5432.
35. N. Tullini, G. Rebecchi, F. Laudiero, Reliability of the tensile force identification in ancient tie-rods using one flexural mode shape, *Int. J. Archit. Herit.* **13** (3) (2019) 402–410.
36. STRAND7. Release 2.4.6. Pty Ltd. Copyright 2010, http://www.strand7.com.
37. D. Tomàs, J.A. Lozano-Galant, G. Ramos, J. Turmo, Structural system identification of thin web bridges by observability techniques considering shear deformation, *Thin-Walled Struct.* **123** (2018) 282–293.
38. R.T. Barrett, *Fastener Design Manual*, NASA Reference Publication 1228, NASA Lewis Research Center Cleveland, OH, USA (1990).
39. G. Rebecchi, N. Tullini, F. Laudiero, Estimate of the axial force in slender beams with unknown boundary conditions using one flexural mode shape, *J. Sound Vib.* **332** (18) (2013) 4122–4135.
40. C.C. Chen, W.H. Wu, S.Y. Chen, G. Lai, A novel tension estimation approach for elastic cables by elimination of complex boundary condition effects employing mode shape functions, *Eng. Struct.* **166** (2018) 152–166.
41. W.H. Wu, C.C. Chen, Y.C. Chen, G. Lai, C.M. Huang, Tension determination for suspenders of arch bridge based on multiple vibration measurements concentrated at one end, *Measurement* **123** (2018) 254–269.
42. W. Chen, B. Yan, J. Liao, L. Luo, Y. Dong, Cable force determination using phase-based video motion magnification and digital image correlation, *Int. J. Struct. Stab. Dy.* **22** (7) (2022) 2250036.
43. S. Park, T. Kim, K. Kim, S.N. Hong, Flexural behavior of steel I-beam prestressed with externally unbonded tendons, *J. Constr. Steel Res.* **66** (2010) 125–132.

44. Y. Ren, Y. Wang, B. Wang, H. Ban, J. Song, G. Su, Flexural behavior of steel deep beams prestressed with externally unbonded straight multi-tendons, *Thin-Walled Struct.* **131** (2018) 519–530.

45. A. Belletti, A. Gasperi, Behavior of prestressed steel beams, *J. Struct. Eng.* **136** (9) (2010).

46. M.Y. Kim, N. Nanzad, U. Hayat, Effects of un-bonded deviators on the out-of-plane buckling of steel H-beams pre-stressed by a straight tendon cable, *Eng. Struct.* **214** (2020) 110566.

47. M. Saiidi, B. Douglas, S. Feng, Prestress force effect on vibration frequency of concrete bridges, *J. Struct. Eng.* **120** (7) (1994) 2233–2241.

48. Y. Toyota, T. Hirose, S. Ono, K. Shidara, Experimental study on vibration characteristics of prestressed concrete beam, *Procedia Eng.* **171** (2017) 1165–1172.

49. M. Gkantou, M. Theofanous, C. Baniotopoulos, A numerical study of prestressed high strength steel tubular members, *Front. Struct. Civ. Eng.* **14** (1) (2020) 10–22.

50. X. Li, S. Wan, Y. Zhang, M. Zhou, Y. Mo, Beam finite element for thin-walled box girders considering shear lag and shear deformation effects, *Eng. Struct.* **233** (2021) 111867.

51. D. Noble, The effect of prestress force magnitude and eccentricity on natural bending frequencies of prestressed concrete structures, Ph.D. thesis, Trinity College (Dublin, Ireland), Department of Civil, Structural and Environmental Engineering (2016) pp. 385.